A half-plane time-domain BEM for *SH*-wave scattering by a subsurface inclusion

Mehdi Panji[*], Saeed Mojtabazadeh-Hasanlouei, Farshid Yasemi

Department of Civil Engineering, Zanjan Branch, Islamic Azad University, Zanjan, 58145-45156, Iran

ABSTRACT

A direct time-domain numerical approach named the half-plane boundary element method is proposed based on the half-space Green's functions for seismic analysis of a homogeneous linear elastic half-plane in presence of arbitrarily shaped subsurface inclusions, subjected to propagating obliquely incident *SH*-waves. It is assumed that inclusion is completely connected to the surrounding domain. In the use of the method, only the interfaces need to be discretized to create the model. First, the problem is decomposed into two parts including a pitted half-plane and a closed filled solid. Then, the influence coefficients of the matrices are obtained by applying the method to each part. By satisfying the boundary/continuity conditions on the interfaces, a coupled equation is finally formed to determine unknown boundary values in each time-step. After implementing the method in an advanced developed algorithm, its efficiency is investigated by solving some practical examples and compared with those of the published works. The results show that the proposed method has an appropriate accuracy for analyzing seismic inclusion problems. To complete the results, the synthetic seismograms of the surface are presented for circular/elliptical subsurface inclusions. Then, three-dimensional amplification patterns are illustrated for some specific cases. The method can be recommended to geotechnical/mechanical engineers for transient analysis of different topographic features, seismic isolation and composite materials.

1. Introduction

Study on the effects of subsurface topographic features such as cavities and inclusions shows the significant role of local conditions on the motions of ground surface due to seismic waves. Thus, the site effects engendered by existence of subsurface irregularities can lead to amplifications/de-amplifications of seismic waves in different parts of the surface (Davis and West, 1973; Sánchez-Sesma, 1987). Therefore, one of the most important issues is to recognize seismic ground motions and damage investigations during an earthquake and in presence of subsurface topographic features (Aki, 1988).

In underground non-homogeneities such as inclusions, different impedances of materials compared to the surrounding domain makes them for having a particular significance among the other subsurface topographic features (Aki, 1993). Thus, modeling of such features using an appropriate approach can present a better attitude for the detection of their seismic behavior (Dravinski, 1983). Technically speaking, there are four proposed approaches for the seismic analysis of the ground surface, which can be divided into analytical, semi-analytical,

experimental and numerical methods. Each of the mentioned approaches has certain advantages and disadvantages to others (Sánchez-Sesma et al., 2002). Among the recent mathematical-based analytical studies can pointed out to the research of Zhang et al. (2019) where presented the site amplification effects of a radially multi-layered semi-cylindrical canyon on seismic response of an earth and rockfill dam utilizing the wave function expansion method. Due to the lack of flexibility of analytical approaches in modeling and analysis of complex topographical features which are visible in nature, the use of numerical methods is inevitable. Although the existence of approximation cannot be neglected in the results of numerical methods which is because of discretizing processes, realistic problems with complex geometries can be modeled utilizing these approaches (Manoogian and Lee, 1996). In fact, in the numerical methods, never can claim that the responses are completely accurate, but the main goal is a convergence towards the exact answers. By dividing the common numerical methods into two general categories, the domain methods and boundary methods can be pointed out. Main domain methods include the finite element method (FEM) and finite difference method (FDM). In the domain

---

* Corresponding author.
  E-mail addresses: m.panji@iauz.ac.ir (M. Panji), mojtabazadeh@iauz.ac.ir (S. Mojtabazadeh-Hasanlouei), farshid.yasemi@iauz.ac.ir (F. Yasemi).
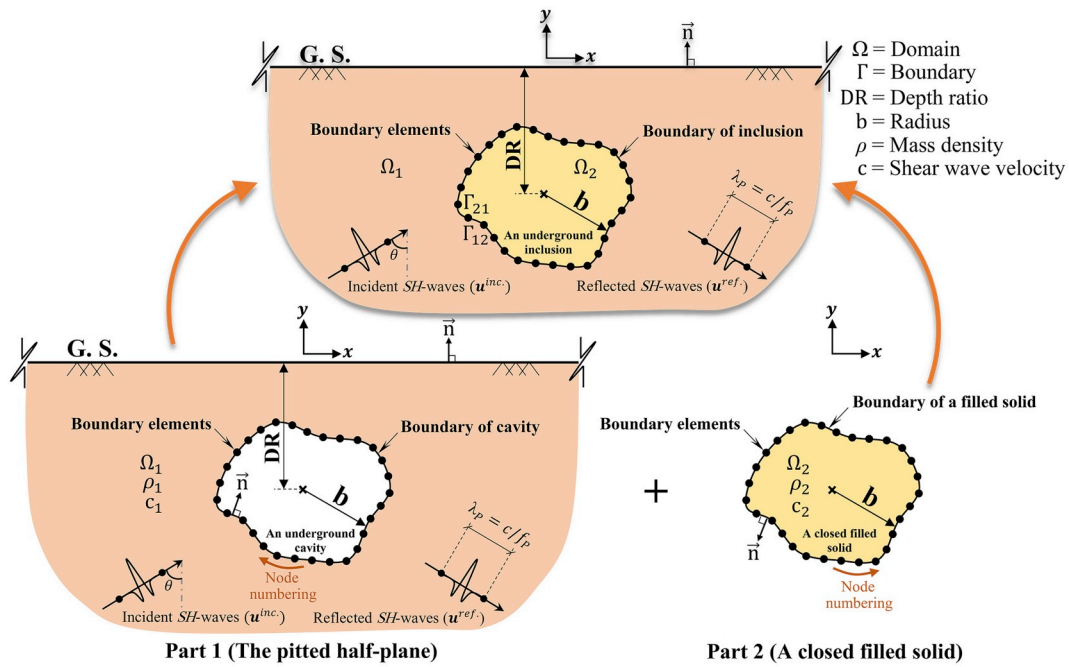
Fig. 1. The problem geometry of an arbitrarily shaped subsurface inclusion placed in an elastic half-plane subjected to the incident *SH*-waves.
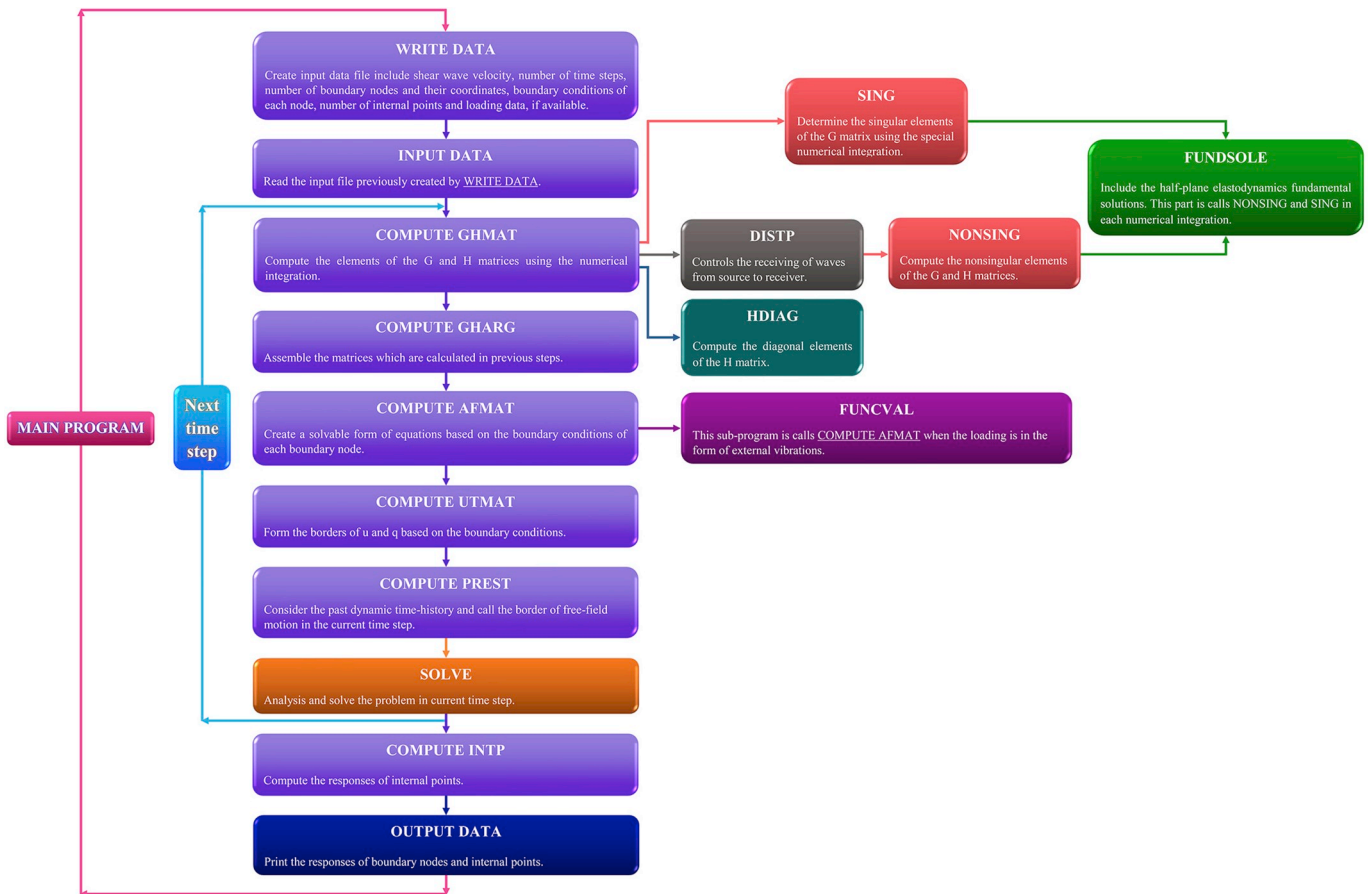

Fig. 2. The flowchart of the DASBEM program for seismic analysis of subsurface inclusion.

methods, the medium of the problem should be closed and the whole the medium should be discretized. Also, the energy absorber should be defined in the corners of the model. Lysmer and Drake (1972), Smith (1975) and Kawase and Sato (1992) were the pioneering researchers who highlighted the application of FEM for seismology and analysis of body wave propagation problems, respectively. The studies of Boore
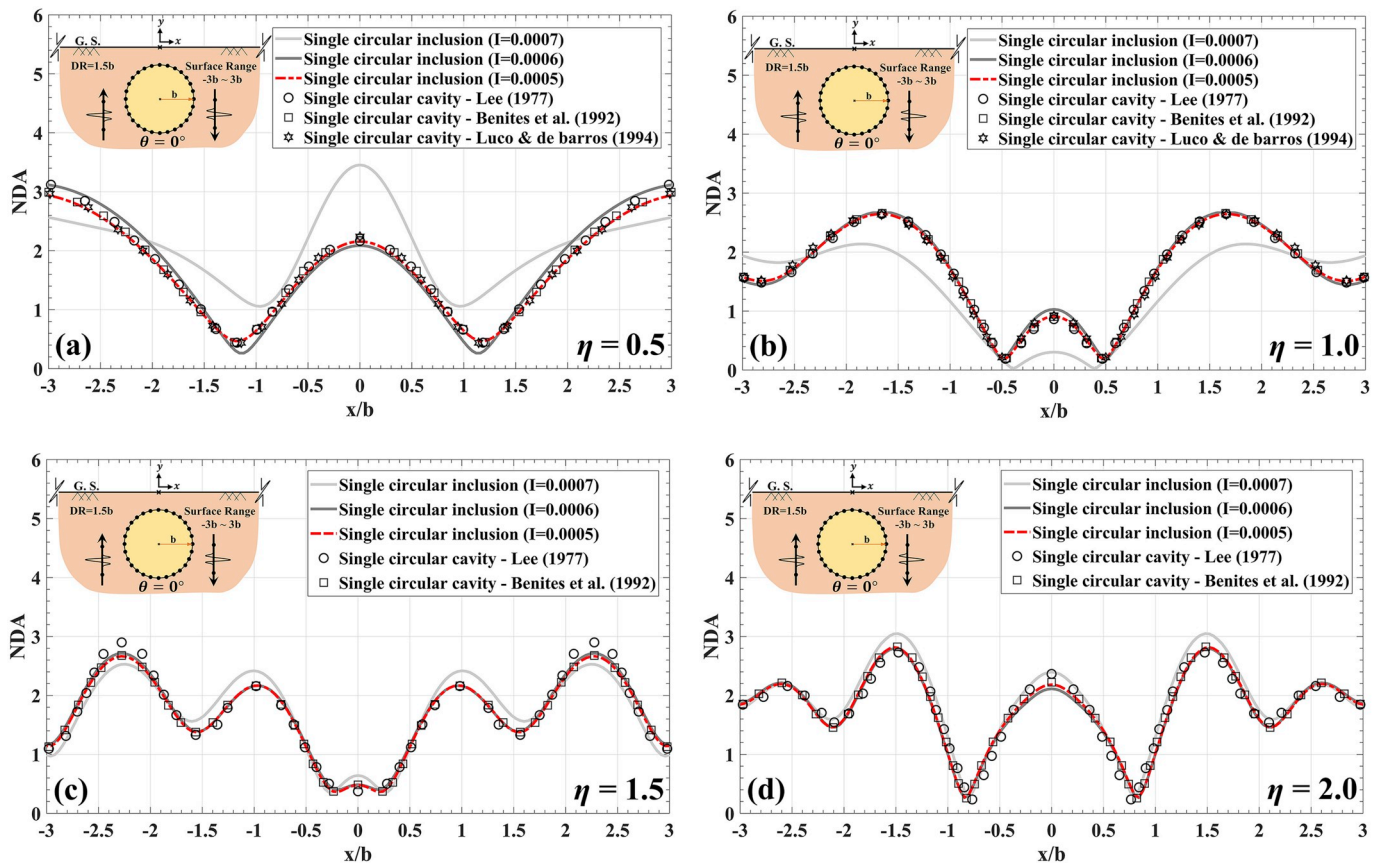
Fig. 3. The normalized displacement amplitude of the ground surface versus x/b for the model of a circular inclusion with the radius of *b* and DR = 1.5*b* subjected to the *SH*-waves. The incident angle of $\theta = 0°$ for the dimensionless frequencies of (a) $\eta = 0.5$., (b) $\eta = 1.0$, (c) $\eta = 1.5$ and (d) $\eta = 2$.
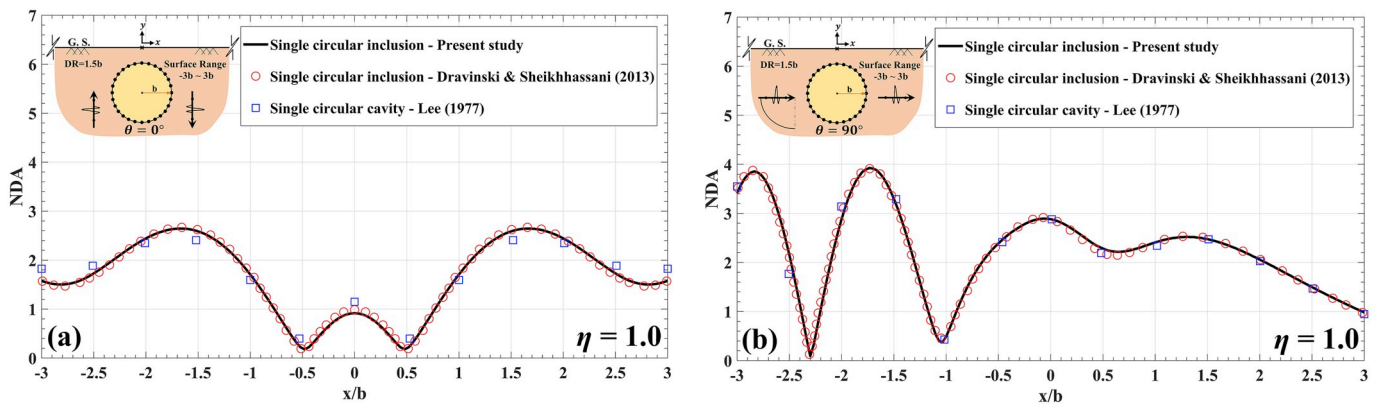

Fig. 4. The normalized displacement amplitude of the ground surface versus x/b for the model of a circular inclusion with the radius of *b* and DR = 1.5*b* subjected to the *SH*-waves with the dimensionless frequency of $\eta = 1.0$ and incident angles (θ) of (a) 0°, (b) 90°.

(1972), Ohtsuki and Harumi (1983) and Moczo and Bard (1993) are the basic studies using FDM that presented the effects of inhomogeneities subjected to seismic *SH*- and *SV*-waves and investigated wave diffraction, amplification and differential motion near strong lateral discontinuities, respectively.

By considering the boundary element method (BEM), one dimension of the models will be reduced and the radiation conditions of waves at infinity will be satisfied. Although BEM approaches include some constraints such as complex formulation and less development in nonlinear, plastic and multiphase media, their use can result in the automatic satisfaction of wave radiation conditions in far boundaries, concentration of meshes only around the boundary of desired topographic features, lower volume of input data, significant reduction in analysis time and extremely high accuracy of exported results due to the large contribution of analytical processes in solving problems (Panji et al., 2013). BEM is divided into two categories including full-plane and half-plane, each being developed in frequency and time-domain. When the full-plane BEM is used, truncating the model from a full-space and discretizing it in a distance far away from the desired zone is inevitable. This leads to satisfaction of stress-free conditions on the ground surface in an approximate process (Ahmad and Banerjee, 1988). Panji et al. (2011) and Panji et al. (2016) used the static full-plane BEM in their studies to evaluate effective parameters on the stability of underground and shallow tunnels subjected to eccentric loads, respectively. Utilizing
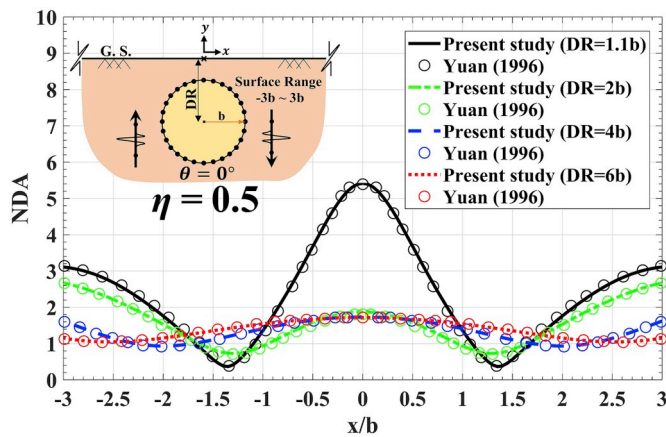
Fig. 5. The normalized displacement amplitude of the ground surface versus x/b for the model of a circular inclusion with the radius of *b* and different DR values subjected to the *SH*-waves with the incident angle of $\theta = 0°$ for the dimensionless frequency of $\eta = 0.5$.

Fig. 6. The normalized displacement amplitude of the ground surface versus x/b for the model of a circular inclusion with the radius of *b* and different DR values subjected to the *SH*-waves with the incident angle of $\theta = 90°$ for the dimensionless frequency of $\eta = 0.5$.
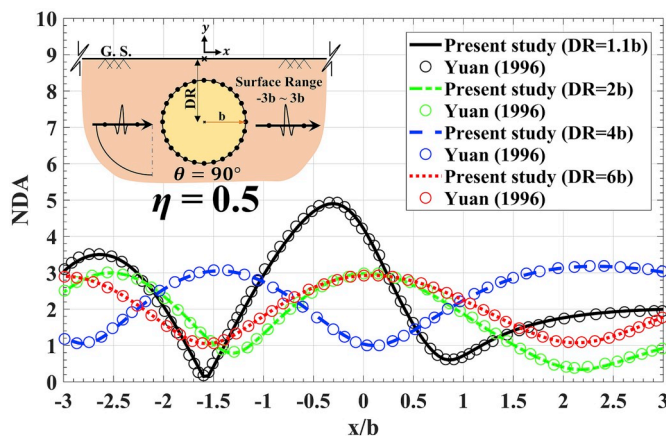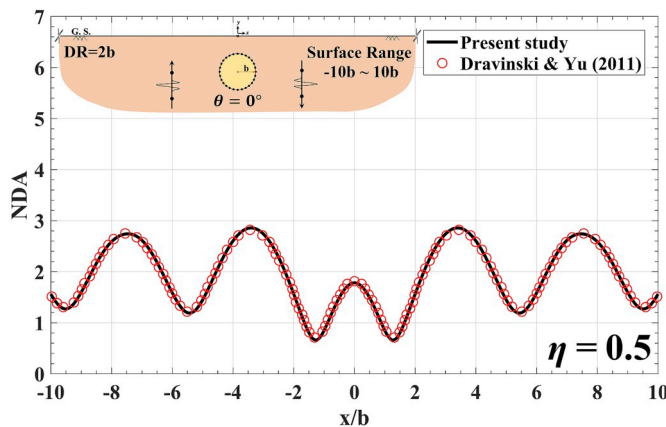

Fig. 7. The normalized displacement amplitude of the ground surface versus x/b for the model of a circular inclusion with the radius of *b* and subjected to the *SH*-waves with the incident angle of $\theta = 0°$ for the dimensionless frequency of $\eta = 0.5$.

the dynamic full-plane BEM, Parvanova et al. (2014) and Parvanova et al. (2015) investigated the dynamic responses of a medium with multiple inclusions under anti-plane strain conditions and wave scattering by nano-heterogeneities embedded in an elastic matrix, respectively. In the half-plane BEM approach, the implementation of the formulation will be more difficult compared to the full-plane BEM. This is because of the satisfaction of stress-free boundary conditions of the ground surface in the formulations. Despite creating bulky equations in the half-plane BEM, there is no need to discretize the smooth surface and define fictitious elements for enclosing boundaries which will help to make the models simpler. Like the previously mentioned approach, the half-plane BEM has been also used for static (Panji and Ansari, 2017a) and dynamic (Dong et al., 2004) analysis of subsurface topographic features as well as underground cavities, pipes and inclusions.

Among the pioneering studies using time-domain BEM are the researches of Rice and Sadd, (1984) who exhibited the propagation of *SH*-waves in semi-infinite domains and Belytschko and Chang (1988) who presented a simplified direct time integration boundary element method. Subsequently, Takemiya and Fujiwara (1994) illustrated the scattering and propagation of *SH*-waves at irregular sites. Then, Feng et al. (2003), Huang et al. (2005) and Mykhaskiv (2005) focused their studies on 2D transient scattering of *SH*-waves from an inclusion with a unilateral frictional interface. In the study of Kamalian et al. (2003), the topic of site response analysis of topographic structures by a 2D time-domain BEM was presented. Moreover, the 2D time-domain site response of nonhomogeneous topographic structures was discovered by Kamalian et al. (2006) using a hybrid FE/BE method. In the following years, the transient analysis of wave propagation problems by the half-plane BEM was carried out by Panji et al. (2013), Panji et al. (2014a, b). Moreover, Ba and Yin (2016) discovered the wave scattering of the complex local site of layered half-space subjected to incident plane *SH*-waves using a multi-domain IBEM. Then, transient *SH*-wave scattering by the lined tunnel embedded in an elastic half-plane was presented by Panji and Ansari (2017b). In another study, Panji and Mojtabazadeh-Hasanlouei (2018) illustrated the time-domain responses of the surface subjected to incident *SH*-waves in presence of regularly distributed enormous embedded cavities. Moreover, using the indirect boundary integral equation method, Liang et al. (2019) studied the broadband scattering of plane *P*, *SV* and *Rayleigh*-waves by a hill topography. Utilizing the same approach, Huang et al. (2019) presented the scattering of plane *P* and *SV*-waves by twin lining tunnels with imperfect interfaces embedded in an elastic half-space. Recently, Panji and Mojtabazadeh-Hasanlouei (2020) focused their research on the transient response of irregular surface by periodically distributed semi-sine shaped valleys subjected to *SH*-waves.

As the literature review shows, the scattering of transient *SH*-waves on the ground surface in the presence of sub-surface inclusion has not yet been directly analyzed in the time-domain. In previous researches, the models were limited to the homogeneous single-material subsurface problems. Although in some researches including Lubich (1988), Garcia-Sanchez and Zhang (2007) and Manolis et al. (2017), the mathematical formulation, numerical implementation and transient analysis of two-dimensional non-homogeneous solids were presented as well, they were established to obtain the time-domain responses by the inverse Fourier/Laplace-transform algorithm from mechanical problems point of view. But, in this study step-by-step transient analysis of arbitrarily shaped subsurface inclusions are presented subjected to propagating obliquely incident plane *SH*-waves using the direct half-plane time-domain BEM approach. In the present paper, the models are developed to heterogeneous state and made up of two separate parts including a pitted half-plane and the medium of alluvium that are assembled on each other. By implementing the proposed method in the general DASBEM algorithm (Panji et al., 2013), its validity was evaluated by analyzing several practical examples. To complete numerical results, some synthetic seismograms and three-dimensional (3D) amplification patterns were also presented to show the surface response
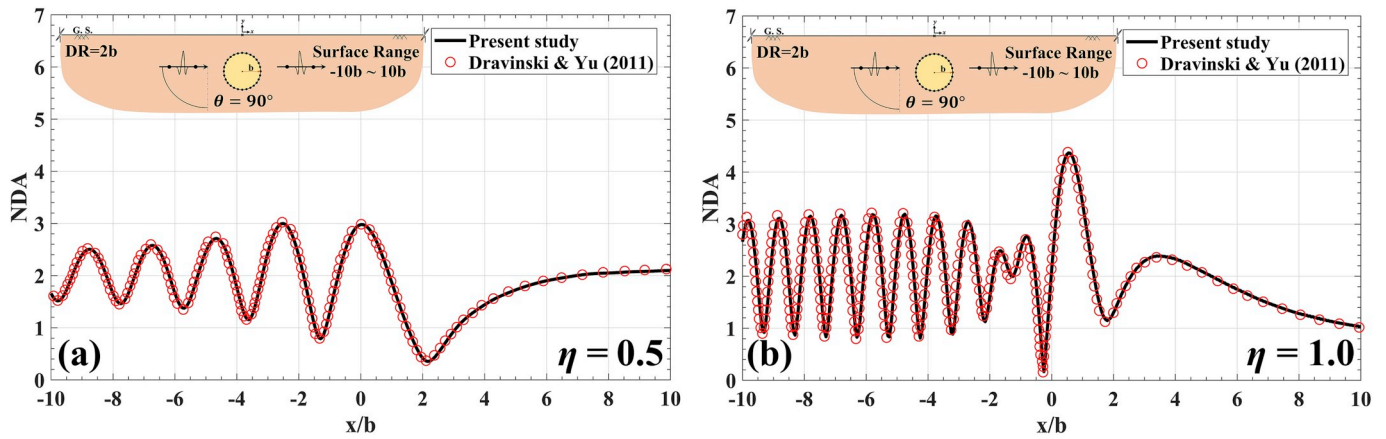
Fig. 8. The normalized displacement amplitude of the ground surface versus x/b for the model of a circular inclusion with the radius of b and subjected to the *SH*-waves with the incident angle of $\theta = 90°$ for the dimensionless frequency of.(a) $\eta = 0.5$, (b) $\eta = 1.0$.
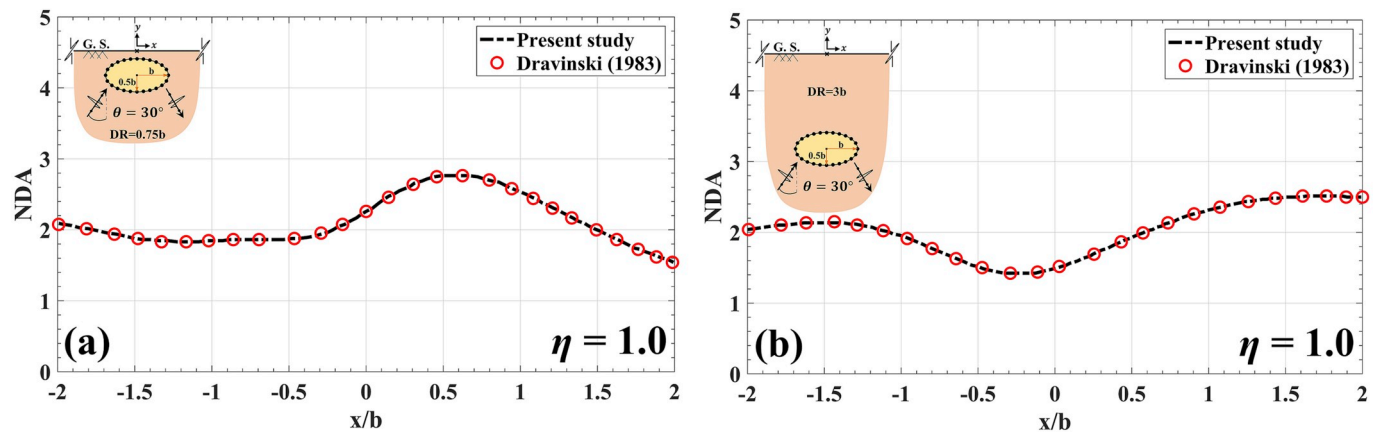

Fig. 9. The normalized displacement amplitude of the ground surface versus x/b for the model of a circular inclusion with the radius of b and different DR values subjected to the *SH*-waves with the incident angle of $\theta = 30°$ for the dimensionless frequency of $\eta = 1.0$.

in the presence of circular/elliptical inclusions. In fact, the main purposes of the present paper are to prepare simple seismic heterogeneous models with different behavior of materials, obtain high accuracy responses, achieve low analysis time and input data and combine numerical approaches in a simple way.

2. Problem statement

As illustrated in Fig. 1, a linear elastic homogeneous and isotropic half-plane is considered as the medium of the models and an arbitrarily shaped subsurface inclusion is located in this medium. As depicted in this figure, Γ is the boundary of the body which is defined separately for the pitted area and the closed solid which will fill the inclusion medium. DR is the depth ratio of inclusion and b is the radius of inclusion. Moreover, Ω is the domain and subscripts of 1 and 2 related to the medium and inclusion, respectively. Moreover, θ is the angle of the incident waves and the parameter n is the normal vector that is perpendicular to the surface and dependent to the node numbering direction. The models are subjected to the incident out-of-plane *SH*-waves of the Ricker type (Panji et al., 2013). The function of a Ricker wavelet type is defined as Eq. (1) (Ricker, 1953):

$$f(t) = \left[1 - 2\left(\pi f_p(t - t_0)\right)^2\right] e^{-\left(\pi f_p(t - t_0)\right)^2} , \tag{1}$$

In Eq. (1), f_p is the predominant frequency of the wave and t_0 is the time shifting parameter. Since the modeling is completely conducted in half-

plane and the stress-free boundary conditions of the ground surface are satisfied, free-field displacement (u^{ff}) can be obtained by adding the phase of the incident and reflected waves as follows (Reinoso et al., 1993):

$$u^{ff}(x, y, t) = \alpha_{max} \cdot \left(\left[1 - 2\left(\frac{\pi f_p}{c}\alpha^{inc.}\right)^2\right] e^{-\left(\frac{\pi f_p}{c}\alpha^{inc.}\right)^2} H\left(t - \frac{r^{inc.}}{c}\right) \right.$$

$$\left. + \left[1 - 2\left(\frac{\pi f_p}{c}\alpha^{ref.}\right)^2\right] e^{-\left(\frac{\pi f_p}{c}\alpha^{ref.}\right)^2} H\left(t - \frac{r^{ref.}}{c}\right) \right) , \tag{2}$$

where $\alpha^{inc.}$, $\alpha^{ref.}$, $r^{inc.}$ and $r^{ref.}$ can be achievable from the following equations:

$$\begin{array}{ll} \alpha^{inc.} = c(t - t_0) + r^{inc.} , & r^{inc.} = -\sin(\theta) \cdot x + \cos(\theta) \cdot y , \\ \alpha^{ref.} = c(t - t_0) + r^{ref.} , & r^{ref.} = -\sin(\theta) \cdot x - \cos(\theta) \cdot y , \end{array} \tag{3}$$

On the other hand, the equation of motion for the anti-plane strain model is as follows:

$$\frac{\partial^2 u(x, y, t)}{\partial x^2} + \frac{\partial^2 u(x, y, t)}{\partial y^2} + b(x, y, t) = \frac{1}{c^2}\frac{\partial^2 u(x, y, t)}{\partial t^2} , \tag{4}$$

In Eq. (4), $u(x, y, t)$ and $b(x, y, t)$ are out-of-plane displacement and body force at the point (x, y) and current time t, respectively. Moreover, c is the shear-wave velocity determined by $\sqrt{\mu/\rho}$, where μ is the shear
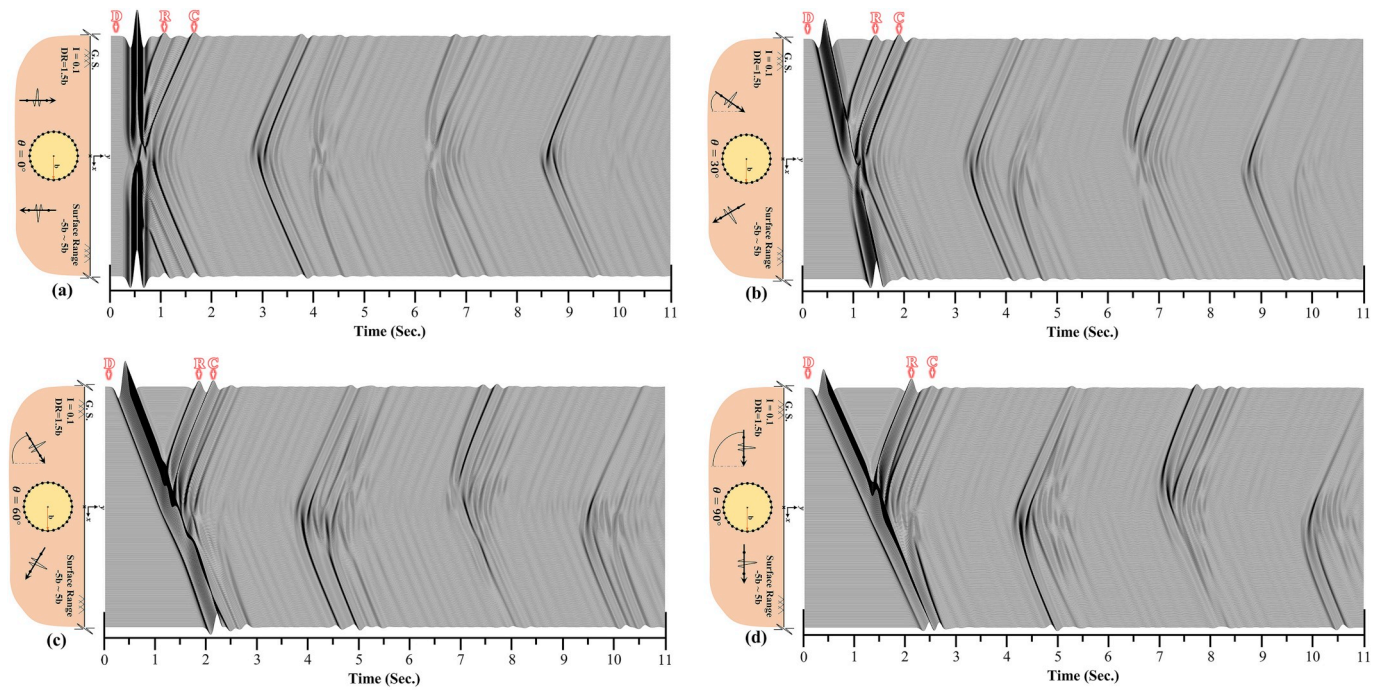
Fig. 10. Synthetic seismograms of the ground surface and the procedure of the *SH*-waves dispersion with time, for the model of a circular inclusion with $I = 0.1$, DR $= 1.5b$ and incident angle of (a) $\theta = 0°$, (b) $\theta = 30°$, (c) $\theta = 60°$ and (d) $\theta = 90°$.

Fig. 11. Synthetic seismograms of the ground surface and the procedure of the *SH*-waves dispersion with time, for the model of a circular inclusion with $I = 0.3$, DR $= 1.5b$ and incident angle of (a) $\theta = 0°$, (b) $\theta = 30°$, (c) $\theta = 60°$ and (d) $\theta = 90°$.

modulus and ρ is the mass density. To obtain a 2D anti-plane semi-infinite medium, Eq. (4) should be solved by the following boundary condition:

$$\frac{\partial u(x, y, t)}{\partial n}\bigg|_{y=0} = 0 , \tag{5}$$

By simultaneously taking the singular solution into account for Eqs. (4) and (5), the half-space Green's functions can be achievable (Panji et al., 2013).

3. Time-domain half-plane boundary element method (BEM)

By utilizing the wave source image technique (Panji et al., 2013) and satisfying the boundary conditions related to the ground surface, one can exclusively concentrate meshes around the boundary of inclusion. The details of this method are mentioned in the following section.
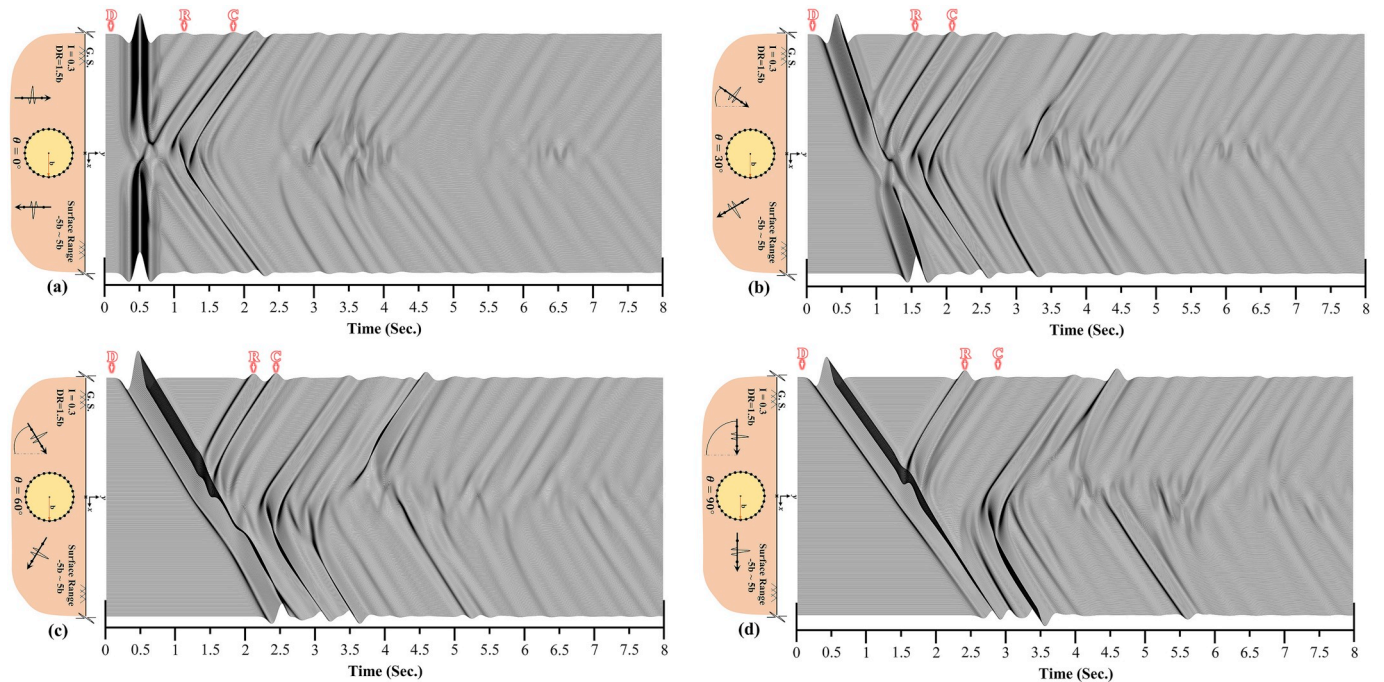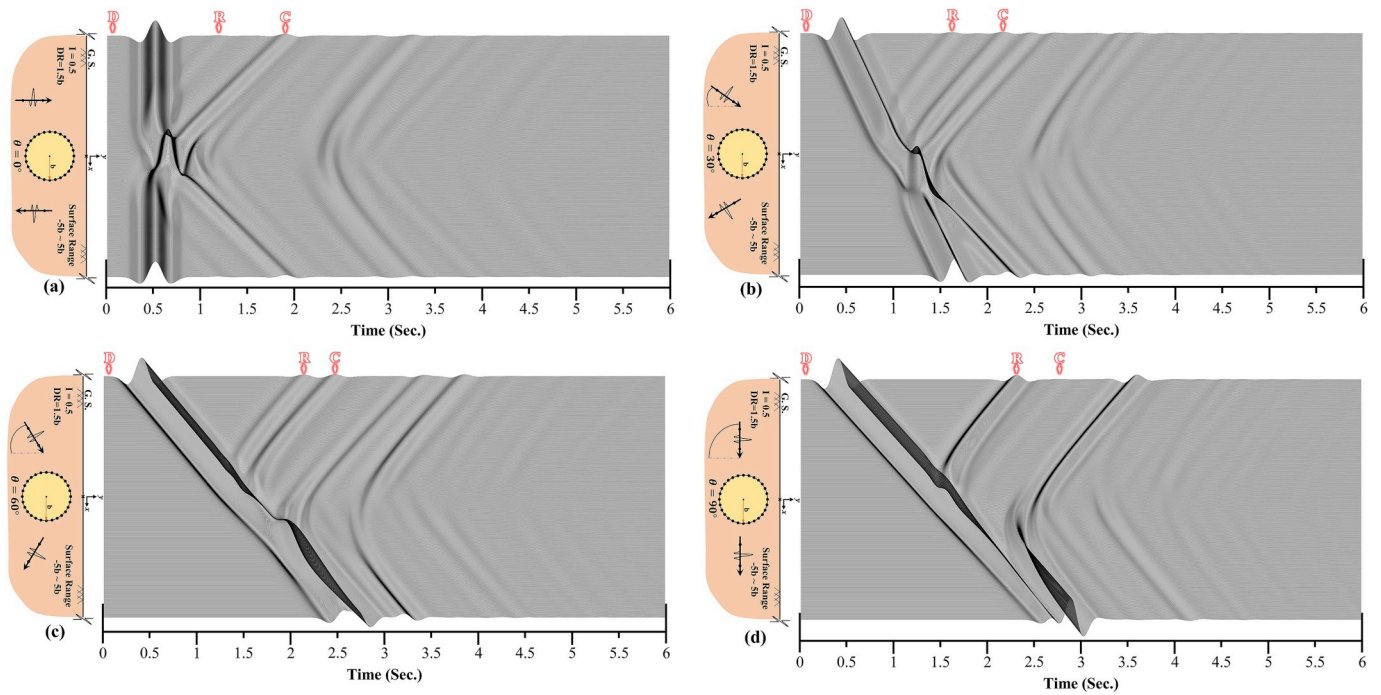
Fig. 12. Synthetic seismograms of the ground surface and the procedure of the *SH*-waves dispersion with time, for the model of a circular inclusion with $I = 0.5$, DR $= 1.5b$ and incident angle of (a) $\theta = 0°$, (b) $\theta = 30°$, (c) $\theta = 60°$ and (d) $\theta = 90°$.

Fig. 13. Synthetic seismograms of the ground surface and the procedure of the *SH*-waves dispersion with time, for the model of an elliptical inclusion with $I = 0.1$, DR $= 1.5b$ and incident angle of (a) $\theta = 0°$, (b) $\theta = 30°$, (c) $\theta = 60°$ and (d) $\theta = 90°$.

3.1. Boundary integral equation (BIE)

At the first step, without considering any boundary condition of Eq. (5), the weighted residual integral is applied on Eq. (4). Then, by carrying out twice integration, eliminating the volumetric integral defined on the domain using boundary methods and ignoring the contributions of the initial conditions and body forces, the direct boundary integral equation (BIE) in the time-domain can be obtained as Eq. (6) (Brebbia

and Dominguez, 1989; Dominguez, 1993; Reinoso et al., 1993):

$$c(\xi)u(\xi, t) = \int_{\Gamma} \left\{ \int_0^t [u^*(x, t; \xi, \tau) \cdot q(x, t) - q^*(x, t; \xi, \tau) \cdot u(x, t)] d\tau \right\} d\Gamma(x) ,$$

(6)

In Eq. (6), u^* and q^* are the half-space displacement and traction Green's functions of the time-domain, respectively (Panji et al., 2013).
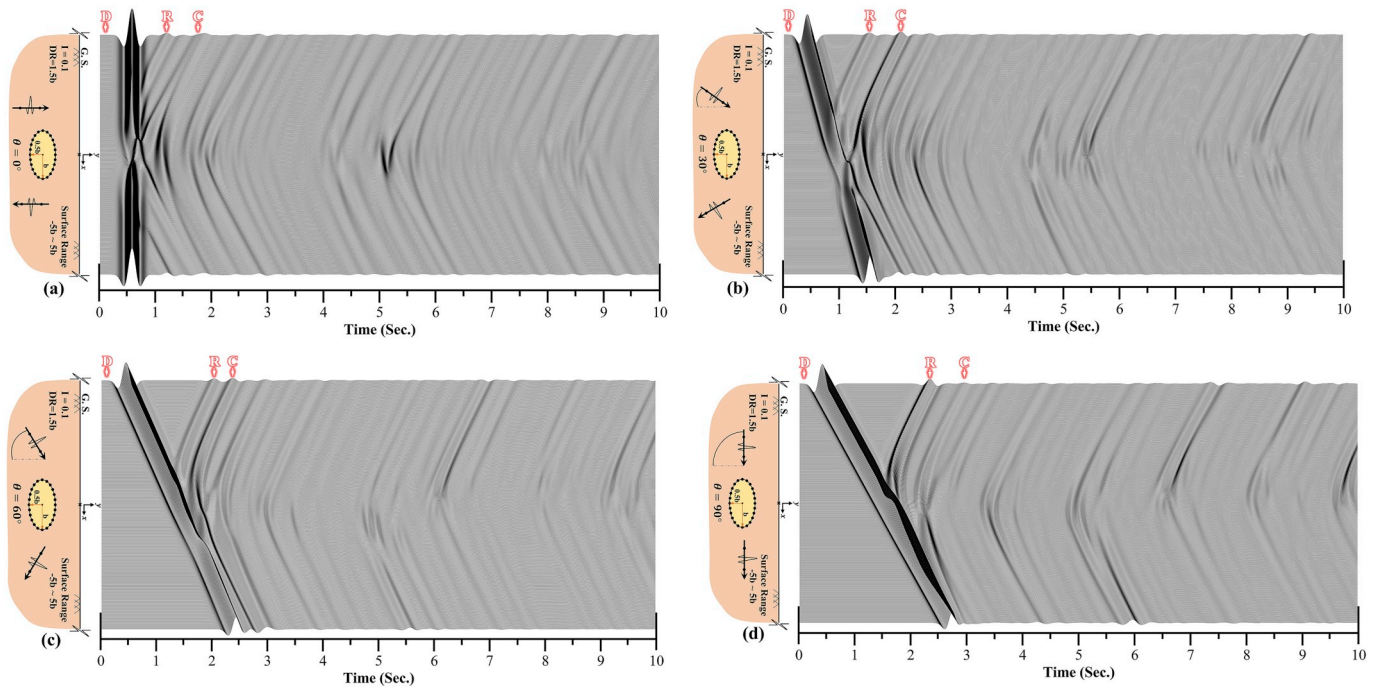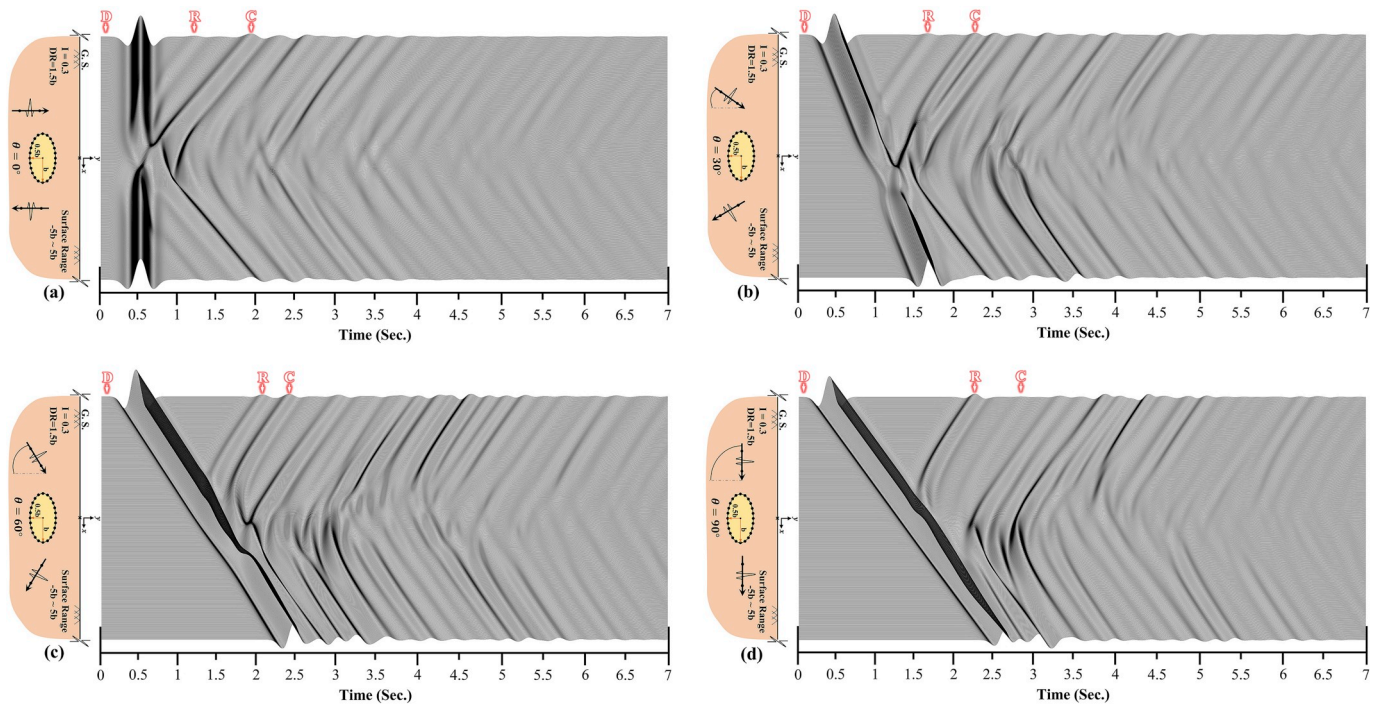
Fig. 14. Synthetic seismograms of the ground surface and the procedure of the *SH*-waves dispersion with time, for the model of an elliptical inclusion with $I = 0.3$, DR $= 1.5b$ and incident angle of (a) $\theta = 0°$, (b) $\theta = 30°$, (c) $\theta = 60°$ and (d) $\theta = 90°$.
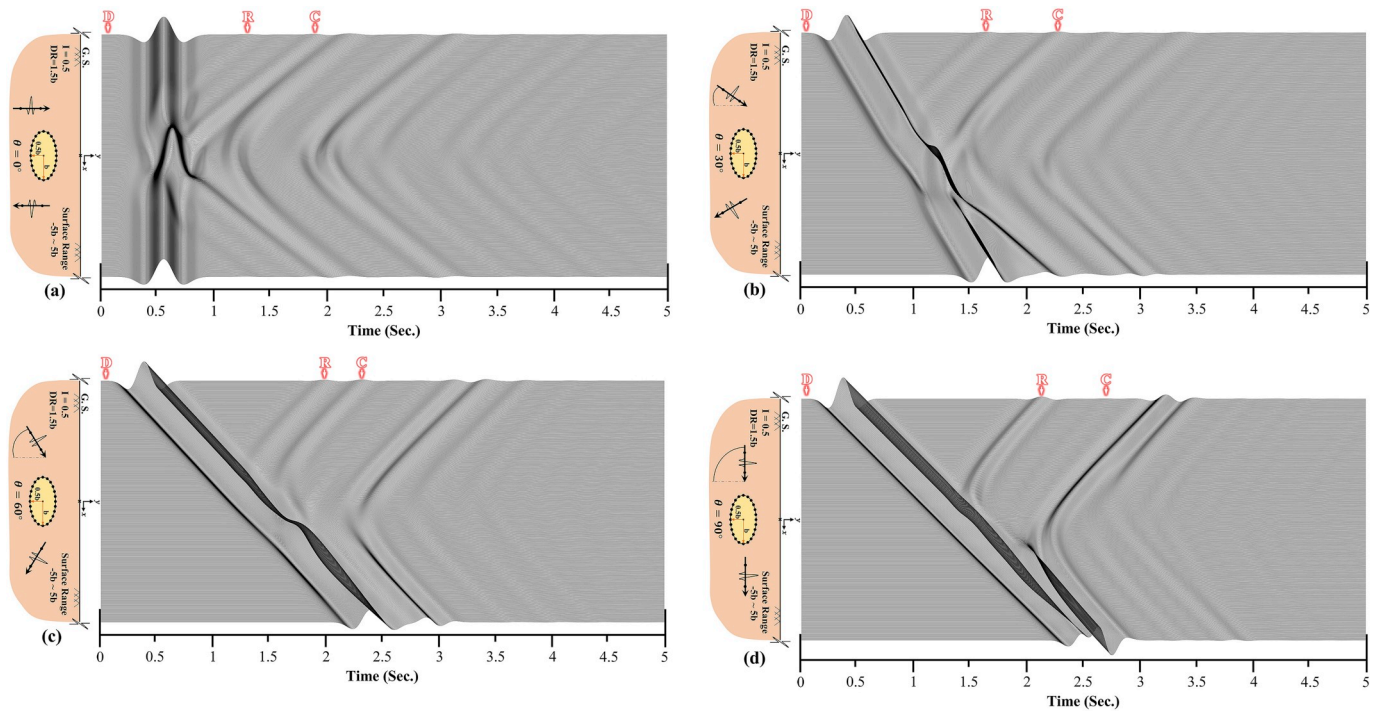
Fig. 15. Synthetic seismograms of the ground surface and the procedure of the *SH*-waves dispersion with time, for the model of an elliptical inclusion with $I = 0.5$, DR $= 1.5b$ and incident angle of (a) $\theta = 0°$, (b) $\theta = 30°$, (c) $\theta = 60°$ and (d) $\theta = 90°$.

Moreover, u and q are the displacements and traction fields on the boundary, respectively, Γ denotes the boundary, and x and ξ are the coordinates of source and receiver, respectively. Additionally, $u^* \cdot q$ and $q^* \cdot u$ are the Riemann-convolution integrals and $c(\xi)$ is the angle of boundary refraction which is defined as the geometry coefficient (Dominguez, 1993). The BIE (6) can be modified to BIE (7) for the total

displacement by insertion of the free-field displacement on the ground surface in the half-plane without presence of any irregularities (Kawase, 1988; Hadley et al., 1989).

Fig. 16. The 3D amplification of the ground surface versus different dimensionless frequencies for the model of a circular inclusion subjected to the *SH*-waves with $I = 0.3$, DR = 1.5b and the incident angle of (a) $\theta = 0°$, (b) $\theta = 30°$, (c) $\theta = 60°$, and (d) $\theta = 90°$.

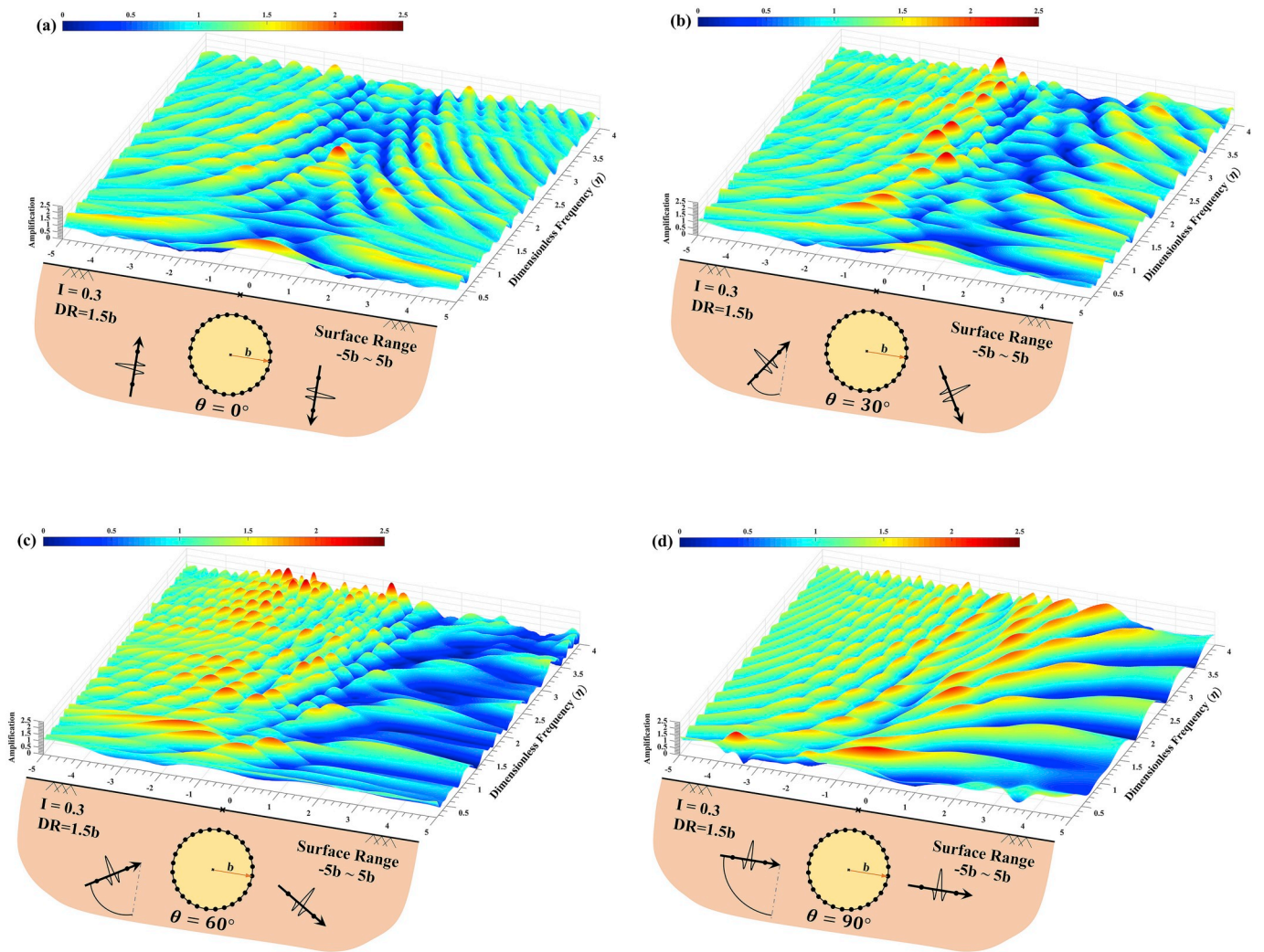$$c(\xi)u(\xi,t) = \int_{\Gamma} \left\{ \int_0^t [u^*(x,t;\xi,\tau) \cdot q(x,t) - q^*(x,t;\xi,\tau) \cdot u(x,t)] d\tau \right\} d\Gamma(x) + u^{ff}(\xi,t) , \tag{7}$$

where u^{ff} is the free-field displacement on ground surface without presence of any irregularities. By solving Eq. (7), total displacement due to presence of inclusion can be obtained. In this step, it is possible to obtain displacements at any point m in Ω, including the ground surface ($y = 0$). The following modified equation can be used for internal points. In this step, $c^m(\xi)$ should be equal to 1.0.

$$u^m(\xi,t) = \int_{\Gamma} \left\{ \int_0^t [u^{*m}(x,t;\xi,\tau) \cdot q(x,t) - q^{*m}(x,t;\xi,\tau) \cdot u(x,t)] d\tau \right\} d\Gamma(x) + u^{ff,m}(\xi,t) , \tag{8}$$

in which, the half-space displacement and traction Green's functions for each internal point are shown by u^{*m} and q^{*m}, respectively. Moreover, the free-field displacements are shown by $u^{ff,m}$ that should be recalculated in this step.

4. Numerical implementation

In this step, the time-axis should be considered and the geometric boundary of the body should be discretized before solving Eq. (7) and obtaining field variables. In fact, the mentioned equation is an exact solution until reaching this step and there is no approximation in this equation before applying discretization on the boundaries of the pitted area and closed filled solid. To carry out temporal integration, an analytical process followed by a numerical procedure should be performed to achieve spatial integration.

4.1. Temporal integration

By considering Δt, the time interval will be divided into N equal increments from 0 to t, where $t = N\Delta t$ and field variables can be assumed to remain linear within each time-step. By preparing temporal integrations, the time-convoluted BIE can be rewritten as Eq. (9):

$$c(\xi)u^N(\xi) = \sum_{n=1}^{N} \int_{\Gamma} \left([U_1^{N-n+1}(x,\xi)q^n(x) + U_2^{N-n}(x,\xi)q^n(x)] - [Q_1^{N-n+1}(x,\xi)u^n(x) + Q_2^{N-n}(x,\xi)u^n(x)] \right) d\Gamma(x) + u^{ff,N}(\xi) , \tag{9}$$

in which, U_1^{N-n+1} and U_2^{N-n} are the half-plane displacement time-convoluted kernels and Q_1^{N-n+1} and Q_2^{N-n} are the half-plane traction
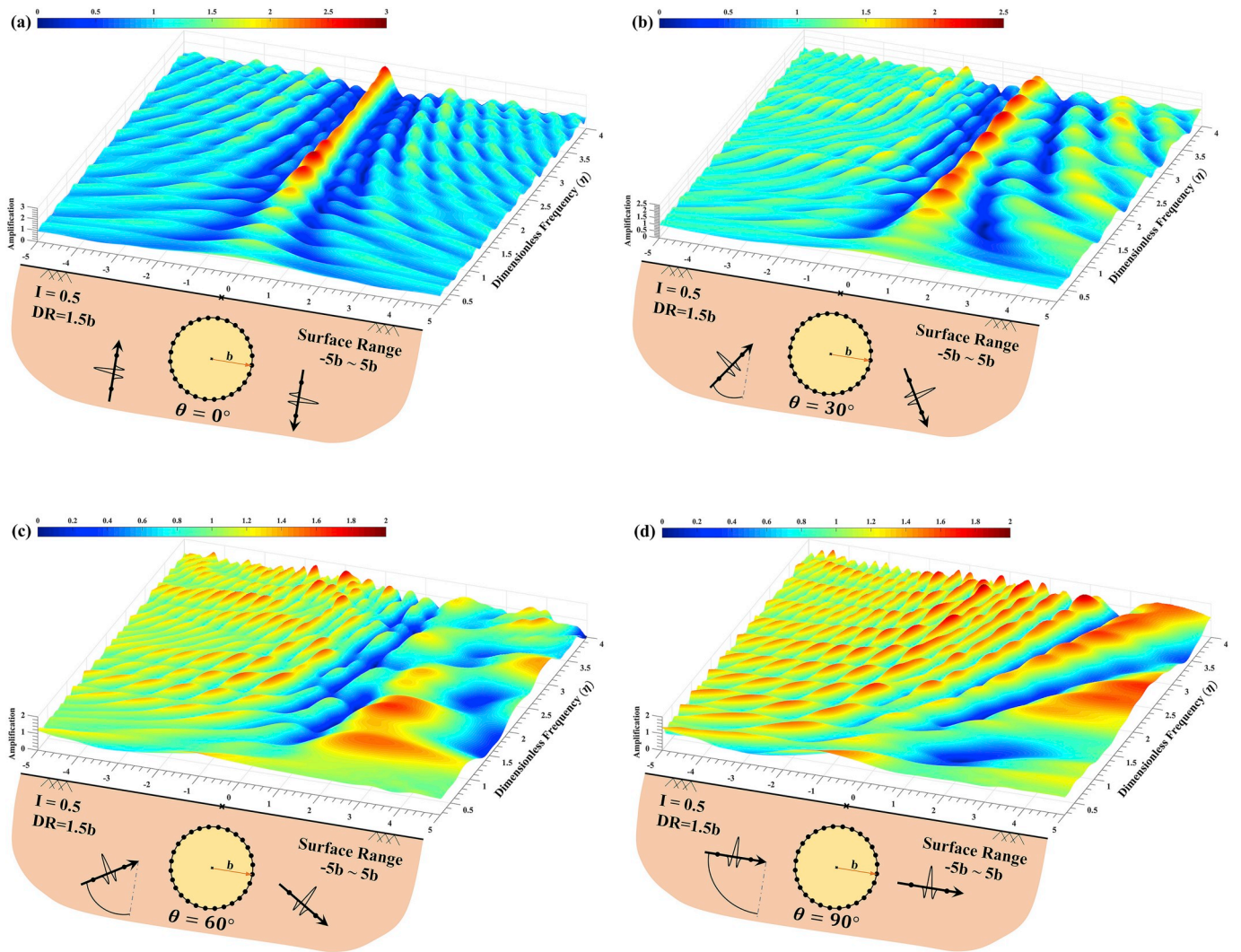
Fig. 17. The 3D amplification of the ground surface versus different dimensionless frequencies for the model of a circular inclusion subjected to the *SH*-waves with $I = 0.5$, DR = $1.5b$ and the incident angle of (a) $\theta = 0°$, (b) $\theta = 30°$, (c) $\theta = 60°$, and (d) $\theta = 90°$.

time-convoluted kernels. These kernels correspond to the forward and backward time-nodes within a time-step, which are shortened in the closed-form. The boundary displacement and free-field displacement are shown as u^N and $u^{ff,N}$, respectively, at the time $t = N\Delta t$. The full form of the time-convoluted kernels of anti-plane elastodynamics for half-plane displacement and traction is presented in Panji et al. (2013).

4.2. Spatial integration

The isoparametric quadratic elements are used to discretize the boundary of the domain for performing the spatial integration in numerical form, and all the related quantities to the geometry and field variables are given in terms of nodal variables.

$$x_i(\kappa) = N_a(\kappa)x_{ia} , \tag{10}$$

$$f(x(\kappa)) = N_a(\kappa)f_a , \tag{11}$$

In these equations, f is the displacement and traction and $N_a(\kappa)$ is the quadratic shape functions, in which κ is the local intrinsic coordinates of the elements. By considering the spatial discretization, Eq. (9) can be rewritten as Eq. (12):

$$c(\xi)u^N(\xi) = \sum_{n=1}^{N} \sum_{m=1}^{M} \left[\int_{\Gamma_m} \left[U_1^{N-n+1}(x(\kappa),\xi) + U_2^{N-n}(x(\kappa),\xi) \right] N_\alpha(\kappa) |J| \, d\kappa \, q_\alpha^n \right.$$
$$\left. - \int_{\Gamma_m} \left[Q_1^{N-n+1}(x(\kappa),\xi) + Q_2^{N-n}(x(\kappa),\xi) \right] N_\alpha(\kappa) |J| \, d\kappa \, u_\alpha^n \right] + u^{ff,N}(\xi) , \tag{12}$$

where $U_1^{N-n+1} + U_2^{N-n}$ and $Q_1^{N-n+1} + Q_2^{N-n}$ are the closed form of scalar half-plane displacement and traction kernels, respectively (Panji et al., 2013). $u^{ff,N}$ and u^N are depicted the free-field motion and displacement field in time step *N*, respectively. Moreover, u^n and q^n are displacement and traction vectors, respectively. In Eq. (12), the total number of boundary elements of inclusion is presented by *M*. The portion of boundary to the element 'm' is indicated by Γ_m and *J* is the Jacobian of transformation. To calculate *J*, Eq. (13) can be used:

$$J_i = \frac{\partial N_\alpha(\kappa)}{\partial \kappa} x_{i\alpha} , \tag{13}$$

4.3. Time-stepping algorithm

By discretizing the geometry boundary of the problem using three-
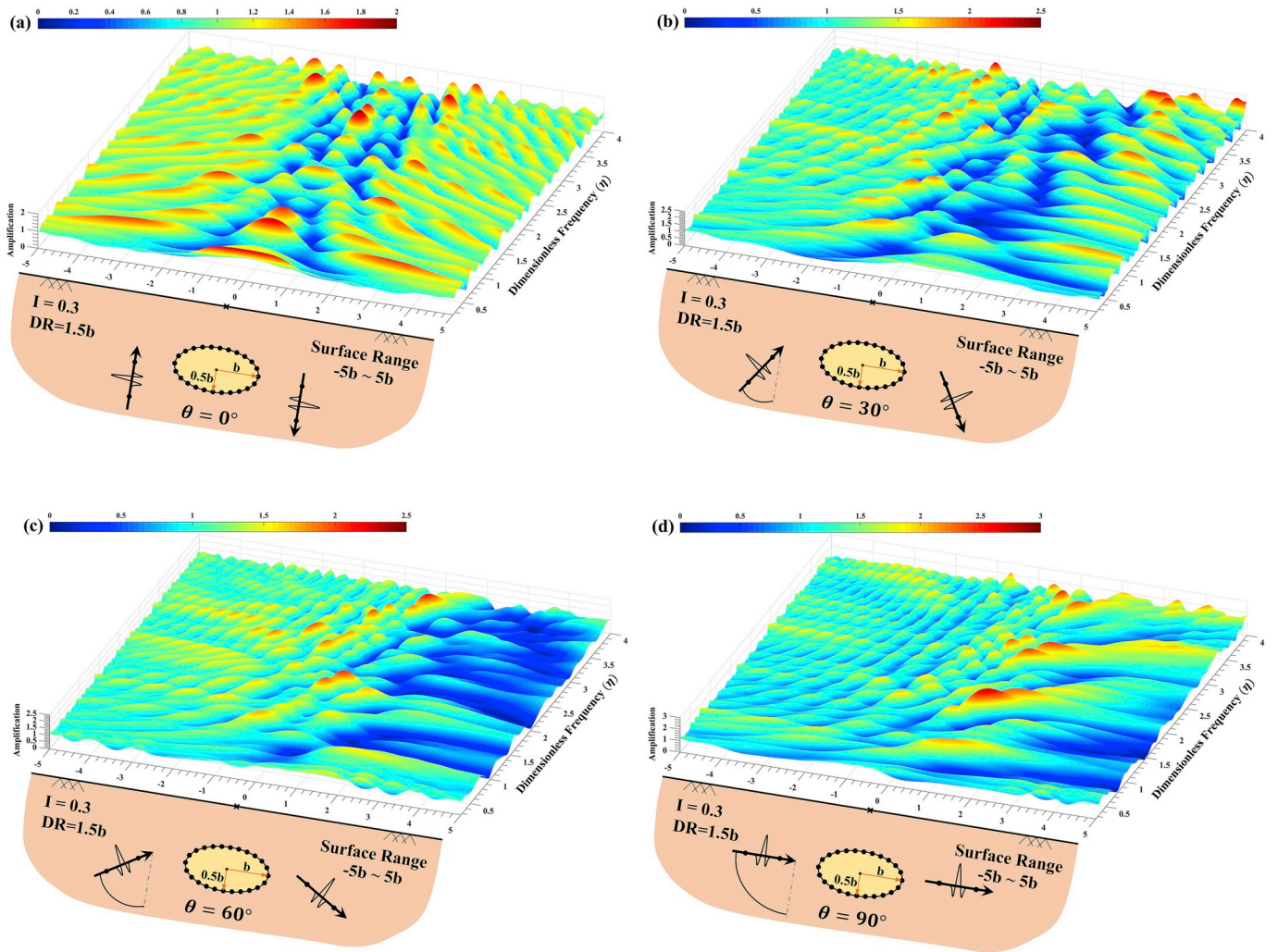
Fig. 18. The 3D amplification of the ground surface versus different dimensionless frequencies for the model of an elliptical inclusion subjected to the *SH*-waves with $I = 0.3$, DR $= 1.5b$ and the incident angle of (a) $\theta = 0°$, (b) $\theta = 30°$, (c) $\theta = 60°$, and (d) $\theta = 90°$.

node quadratic elements and forming the spatial integration of Eq. (12) for all BEs, the following matrix equation can be derived:

$$\sum_{n=1}^{N} H^{N-n+1}\{u^n\} = \sum_{n=1}^{N} G^{N-n+1}\{q^n\} + \{u^{ff,N}\} , \qquad (14)$$

By integration over the boundary elements, the elements of the H^{N-n+1} and G^{N-n+1} matrices can be obtained. The vectors of boundary nodal quantities at the time-step n are shown by $\{u^n\}$ and $\{q^n\}$. When the tractions on the boundary of inclusion are absent, the term $G^{N-n+1}\{q^n\}$ should be considered equal to zero.

$$[A_1^1]\{X^N\} = [B_1^1]\{Y^N\} + \{R^N\} + \{u^{ff,N}\} , \qquad (15)$$

in which:

$$\{R^N\} = \sum_{n=1}^{N-1} \left(G^{N-n+1}\{q^n\} - H^{N-n+1}\{u^n\} \right), \qquad (16)$$

In Eq. (15), $\{X^N\}$ and $\{Y^N\}$ are the vectors including unknown and known variables, respectively, and $\{R^N\}$ includes the effects of past dynamic-history on the current time-node N. By solving Eq. (15), all boundary unknowns at each time-step can be calculated and displacements at the internal point "m" placed into the domain can be obtained.

5. Modeling

According to the sub-structuring process, the subsurface inclusion should be divided into two parts including a pitted half-plane as the first part and a closed filled solid as the second part. The details of modeling are presented in the following sections.

5.1. The first part: the pitted half-plane

This part includes half-plane media with a cavity subjected to the seismic *SH*-waves. If the interface nodes of the cavity connected to the surrounding domain are identified by the subscript of 12, the discretized BIE for this part at the time step N can be written as follows:

$$H_{12}^1 u_{12}^N = G_{12}^1 q_{12}^N + R_{12}^N + u_{12}^{ff,N} , \qquad (17)$$

and in this equation, R_{12}^N is the past dynamic time-history of interface for the first part and in the step N which is defined as follows:

$$R_{12}^N = \sum_{n=1}^{N-1} \left(G_{12}^{N-n+1} q_{12}^n - H_{12}^{N-n+1} u_{12}^n \right) , \qquad (18)$$

Moreover, u_{12}^N is the displacement, q_{12}^N is the traction fields of the interface Γ_{12} belonging to the first part and $u_{12}^{ff,N}$ is the free-field motion of interface nodes.
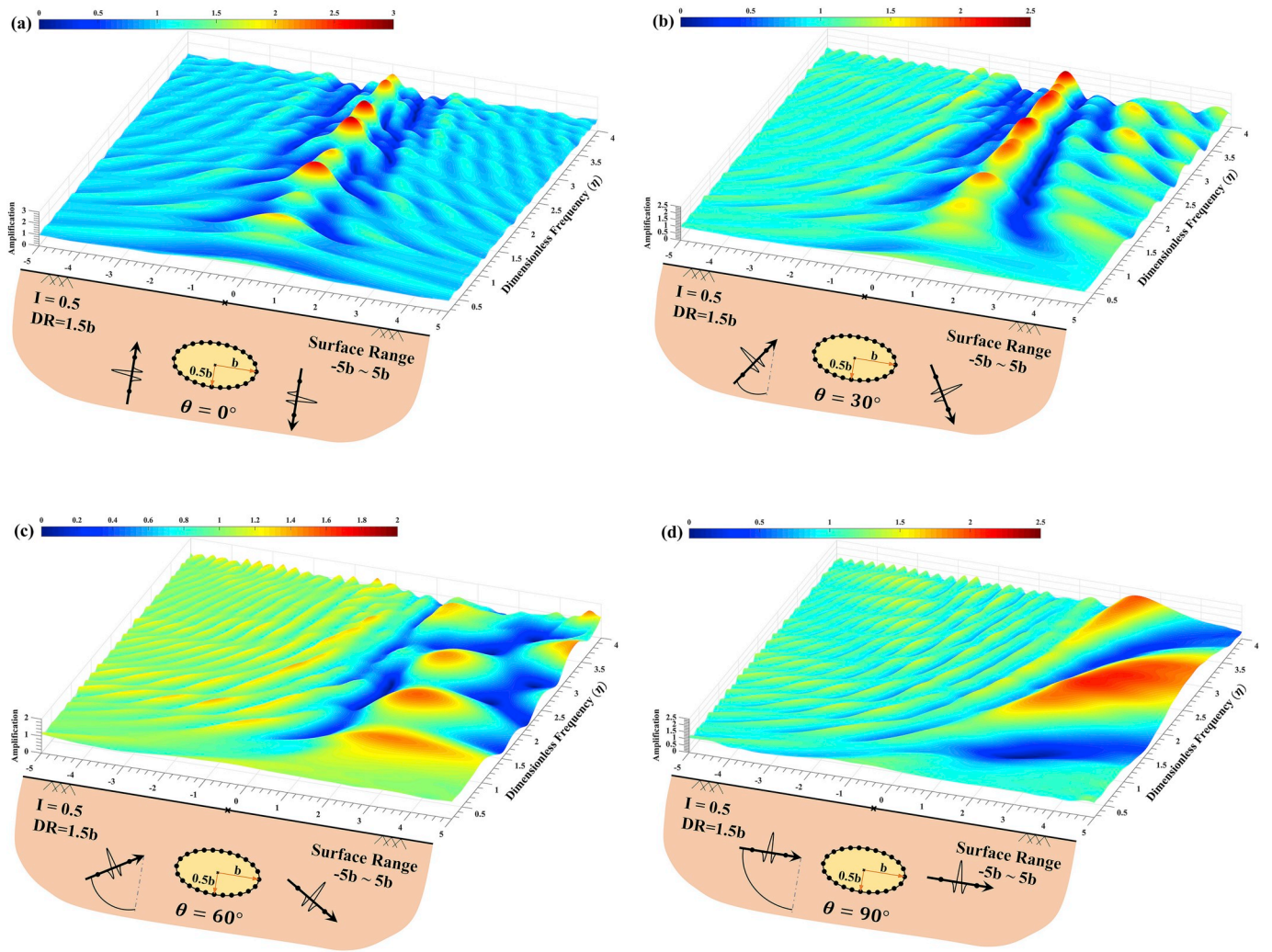
Fig. 19. The 3D amplification of the ground surface versus different dimensionless frequencies for the model of an elliptical inclusion subjected to the *SH*-waves with $I = 0.5$, DR $= 1.5b$ and the incident angle of (a) $\theta = 0°$, (b) $\theta = 30°$, (c) $\theta = 60°$, and (d) $\theta = 90°$.

5.2. The second part: a closed filled solid

This part includes a closed solid medium as the material filling inclusion. The interface nodes of this domain are identified by the subscript of 21, and the discretized BIE at the time step N can be written as follows:

$$H_{21}^1 \, u_{21}^N = G_{21}^1 \, q_{21}^N + R_{21}^N ,\tag{19}$$

in which:

$$R_{21}^N = \sum_{n=1}^{N-1} \left(G_{21}^{N-n+1} q_{21}^n - H_{21}^{N-n+1} u_{21}^n \right) ,\tag{20}$$

where u_{21}^N and q_{21}^N are the displacement and traction fields of the interface Γ_{21} for the second part of the model, respectively. Moreover, R_{21}^N is the past dynamic time-history at the time step N for the interface of the second part.

5.3. Assembling

The equilibrium conditions of displacement and traction compatibility on the interface can be respectively presented as follows:

$$u_{12}^N = u_{21}^N ,\tag{21}$$

and

$$\mu_1 q_{12}^N = -\mu_2 q_{21}^N ,\tag{22}$$

where μ_1 and μ_2 are the shear modulus of the first and second parts of the model, respectively. Finally, by satisfying the mentioned conditions, the final matrix form of the assembled BIEs will be as follows:

$$\begin{bmatrix} H_{12}^1 & -1/\mu_1 \, G_{12}^1 \\ H_{21}^1 & 1/\mu_2 \, G_{21}^1 \end{bmatrix} \begin{Bmatrix} u_{12}^N \\ q_{12}^N \end{Bmatrix} = \begin{Bmatrix} R_{12}^N \\ R_{21}^N \end{Bmatrix} + \begin{Bmatrix} u_{12}^{ff,N} \\ 0 \end{Bmatrix} ,\tag{23}$$

By solving Eq. (23), all unknown values on the interface, such as displacements and tractions, can be obtained. Then, to calculate the displacements of the ground surface, the equations of the first part can be used by assuming $c(\xi) = 1.0$.

6. The DASBEM flowchart

Fig. 2 shows the flowchart of the DASBEM program and its details. This is a program for dynamic analysis of plane scalar time domain problems using half-plane boundary element method (BEM). The mentioned program is developed for analysis of 2D subsurface inclusions embedded in the elastic half-plane. In the following, the download link
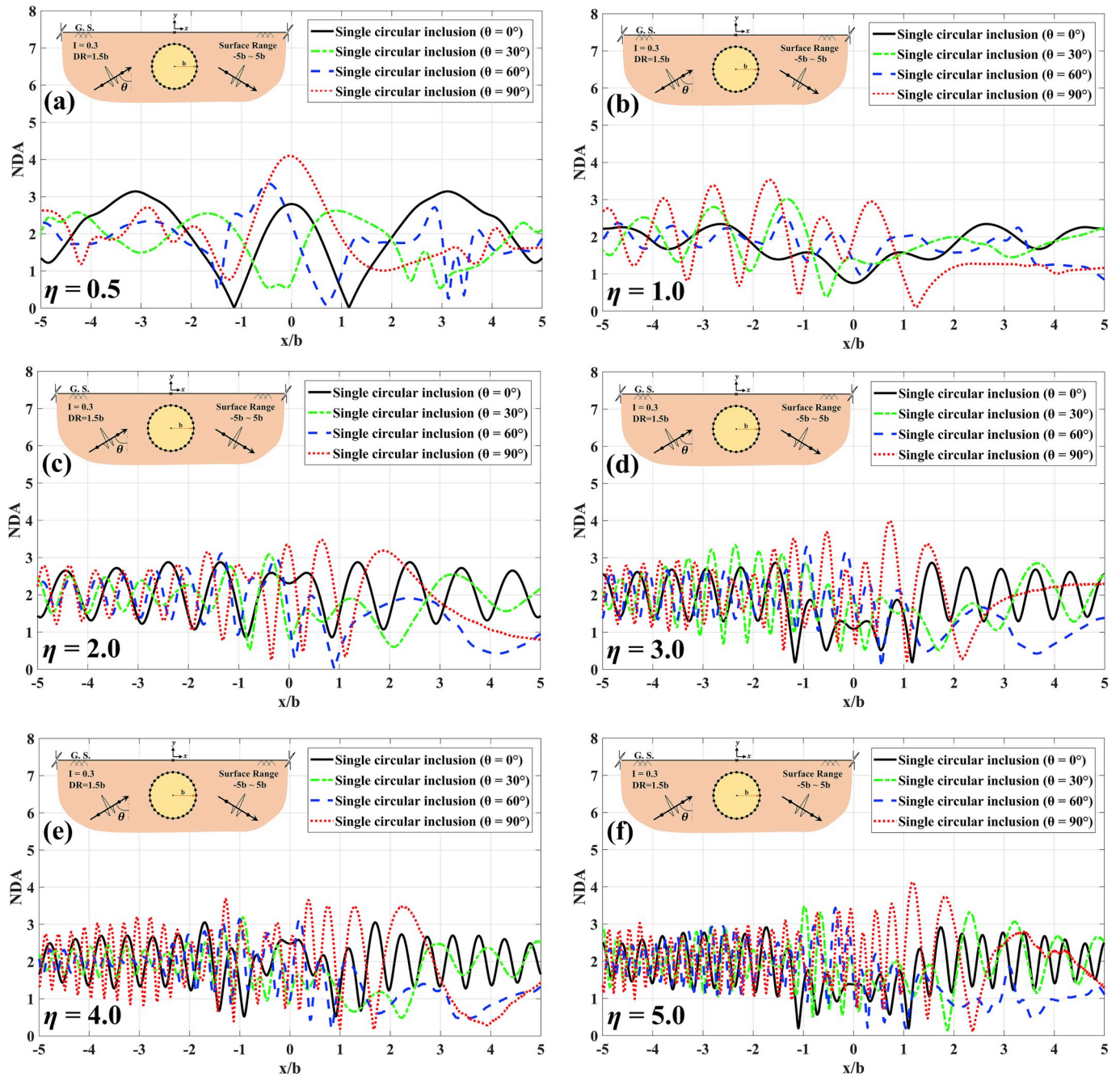
Fig. 20. The normalized displacement amplitude of the ground surface versus x/b for the model of a circular inclusion with the radius of *b* subjected to the *SH*-waves with $I = 0.3$, DR = 1.5*b* for different incident angles and dimensionless frequencies.

of this program is presented and the 'How to use' manual is provided as well (https://github.com/mehdipanji/DASBEM).

7. Application examples

After implementing the above formulation in an algorithm named DASBEM, several practical examples are solved to examine the validity, efficiency and accuracy of the obtained responses. The factor of NDA is the ratio of the Fourier amplitude of the total ground surface motion obtained by BEM for a defined frequency to the Fourier amplitude of the incident motion for the defined frequency. Moreover, the dimensionless frequency (η) is defined as ($\eta = \omega b/\pi c$) where ω is the angular frequency of the wave, *b* is the radius of inclusion and *c* is the shear-wave velocity. The impedance ratio (*I*) is the stiffness ratio of inclusion material to the

surrounding medium and is explained as ($I = \rho_2 c_2/\rho_1 c_1$), where ρ_2 is the mass density, c_2 is the shear-wave velocity of inclusion and ρ_1 and c_1 are the mass density and shear-wave velocity of the surrounding medium, respectively. The numerical procedure for the validation examples is implemented in MATLAB (2018).

To study the behavior of a single underground inclusion located in an elastic half-plane subjected to the seismic *SH*-waves, some key parameters are considered in the models and their effects are clarified, separately. As shown before in Fig. 1, DR is the depth ratio of inclusion, the value of 1.5*b* is considered in all the models and *b* is the radius of inclusion. The shape of inclusion is considered in circular and elliptical mode. Moreover, the incidence angles (θ) of $0°$, $30°$, $60°$ and $90°$ are applied and the impedance ratios (*I*) of 0.1, 0.3 and 0.5 are considered in the models, respectively. Moreover, the range of the ground surface is
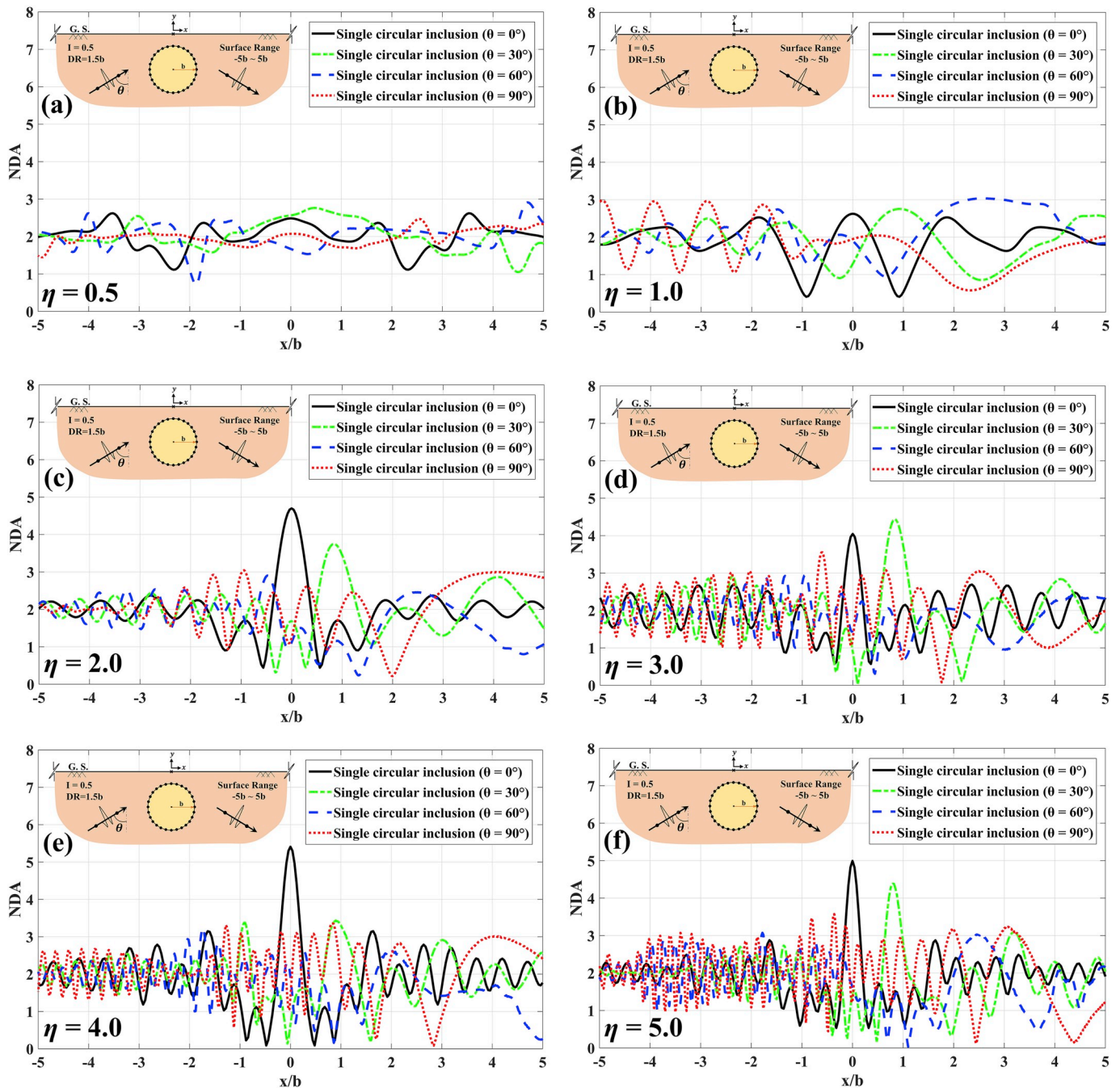
Fig. 21. The normalized displacement amplitude of the ground surface versus x/b for the model of a circular inclusion with the radius of *b* subjected to the *SH*-waves with I = 0.5, DR = 1.5*b* for different incident angles and dimensionless frequencies.

between -5*b* and 5*b*. First, to illustrate the reflections and diffractions of the incident waves, the results of time-domain are presented and then, the responses of frequency-domain in 3D and 2D mode are illustrated for some specific cases to demonstrate the general pattern of amplifications and displacements of the ground surface.

7.1. Verification study

In this section, some different examples are prepared to comparison the obtained results with the solutions presented by other researchers. The details of this examples are mentioned in the following subsections.

7.1.1. Circular weakened inclusion
As depicted in Fig. 3, an extremely soft circular inclusion is modeled

in the depth of 1.5*b* subjected to the incident *SH*-waves. For this purpose, the dimensionless frequencies (η) of 0.5, 1.0, 1.5 and 2.0 as well as the impedance ratios (*I*) of 0.0007, 0.0006 and 0.0005 are considered. The incident *SH*-waves are applied vertically. Based on the different impedance ratios, the shear-wave velocities of (c_2) of 2.52 $m.s^{-1}$, 2.16 $m.s^{-1}$ and 1.8 $m.s^{-1}$ and the mass density (ρ_2) of 0.67 $ton.m^{-3}$ are considered for the material of inclusion, respectively. Moreover, the values of the mentioned parameters for the surrounding medium are 2400 $m.s^{-1}$ and 1 $ton.m^{-3}$. Additionally, the predominant frequency and maximum amplitude of the *SH*-waves of the Ricker wavelet type are equal to 3 Hz and 0.001 m and the time-shifting parameter is equal to 1.7 s. This problem is solved by 1000 time-steps with Δt of 0.004 s. The number of BEs considered for a circular inclusion is equal to 158 elements. By
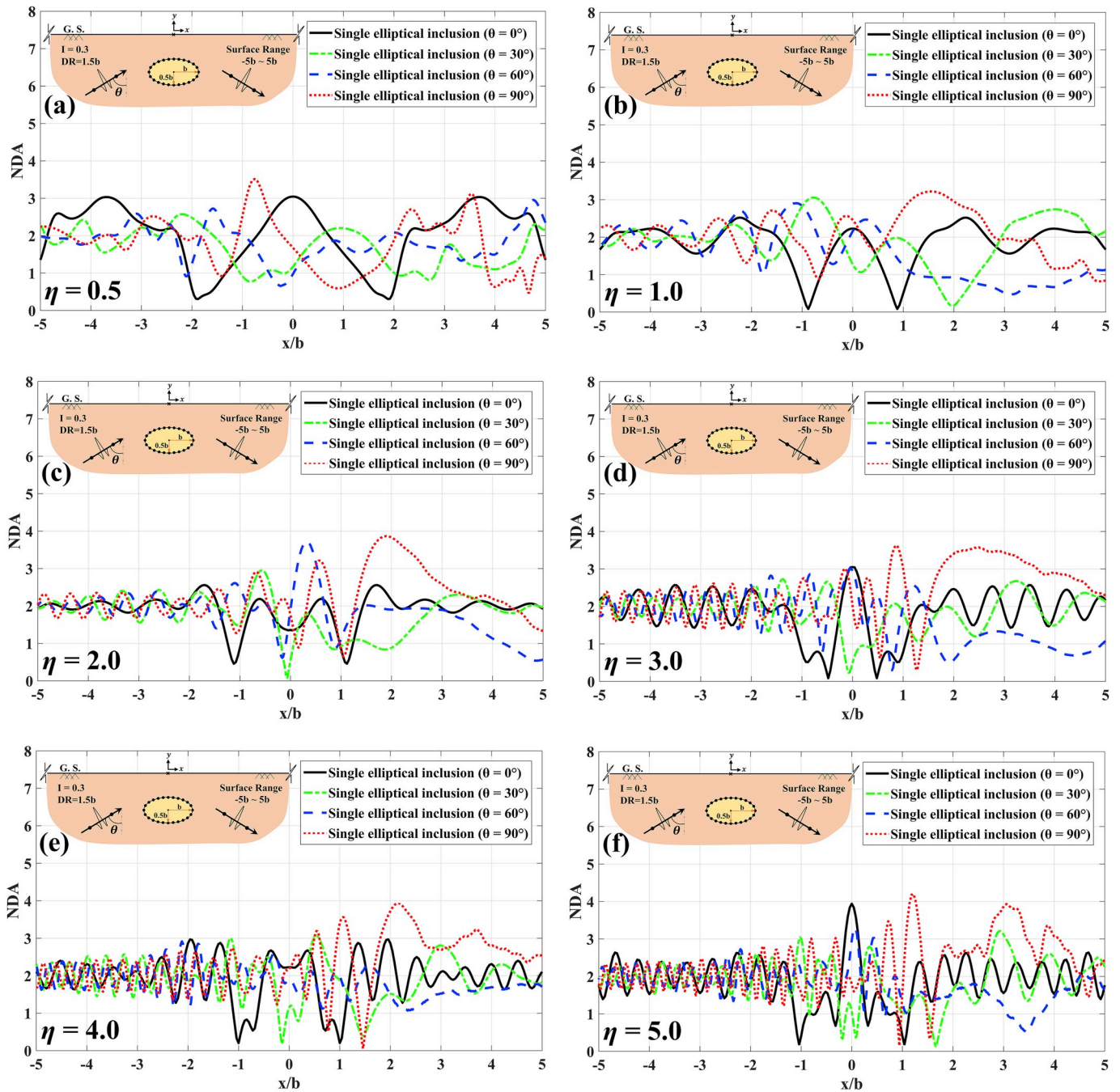
Fig. 22. The normalized displacement amplitude of the ground surface versus x/b for the model of an elliptical inclusion with the radius of *b* subjected to the *SH*-waves with $I = 0.3$, DR = 1.5*b* for different incident angles and dimensionless frequencies.

considering that the behavior of an extremely soft inclusion is similar to the response of a hollow cavity, the results of Lee (1977), Benites et al. (1992) and Luco and de Barros (1994) are used for this verification example. Comparing the obtained results of the present study for the extremely weakened material of inclusion with the analytical solutions of hollow cavities presented by the mentioned researchers illustrates a good agreement for $I = 0.0005$. In another verification example for circular inclusion, the responses of Dravinski and Sheikhhassani (2013) for an extremely soft inclusion are compared to the numerical responses of the present study and also to the analytical results of Lee (1977) for a circular cavity. In the study of Dravinski and Sheikhhassani (2013), the direct frequency-domain full-plane BEM approach was used to show ground surface displacements in presence of an extremely soft circular

inclusion. Fig. 4 shows the normalized displacement amplitude (NDA) of the surface for the incident angles (θ) of 0° and 90°. The effective parameters are considered similar to the previous example, and the obtained diagrams are completely coincident.

7.1.2. Circular inclusion

Figs. 5 and 6 compare the obtained responses of the present study for a subsurface circular inclusion with those presented analytically by Yuan (1996). The depth ratios (DR) of 1.1*b*, 2.0*b*, 4.0*b* and 6.0*b* as well as the incident angles of (θ) of 0° and 90° are considered, respectively. In addition, the dimensionless frequency (η) is equal to 0.5 and the surface range is between -3*b* and 3*b*. Moreover, Figs. 7 and 8 show the numerical results of Dravinski and Yu (2011) obtained using the frequency-domain
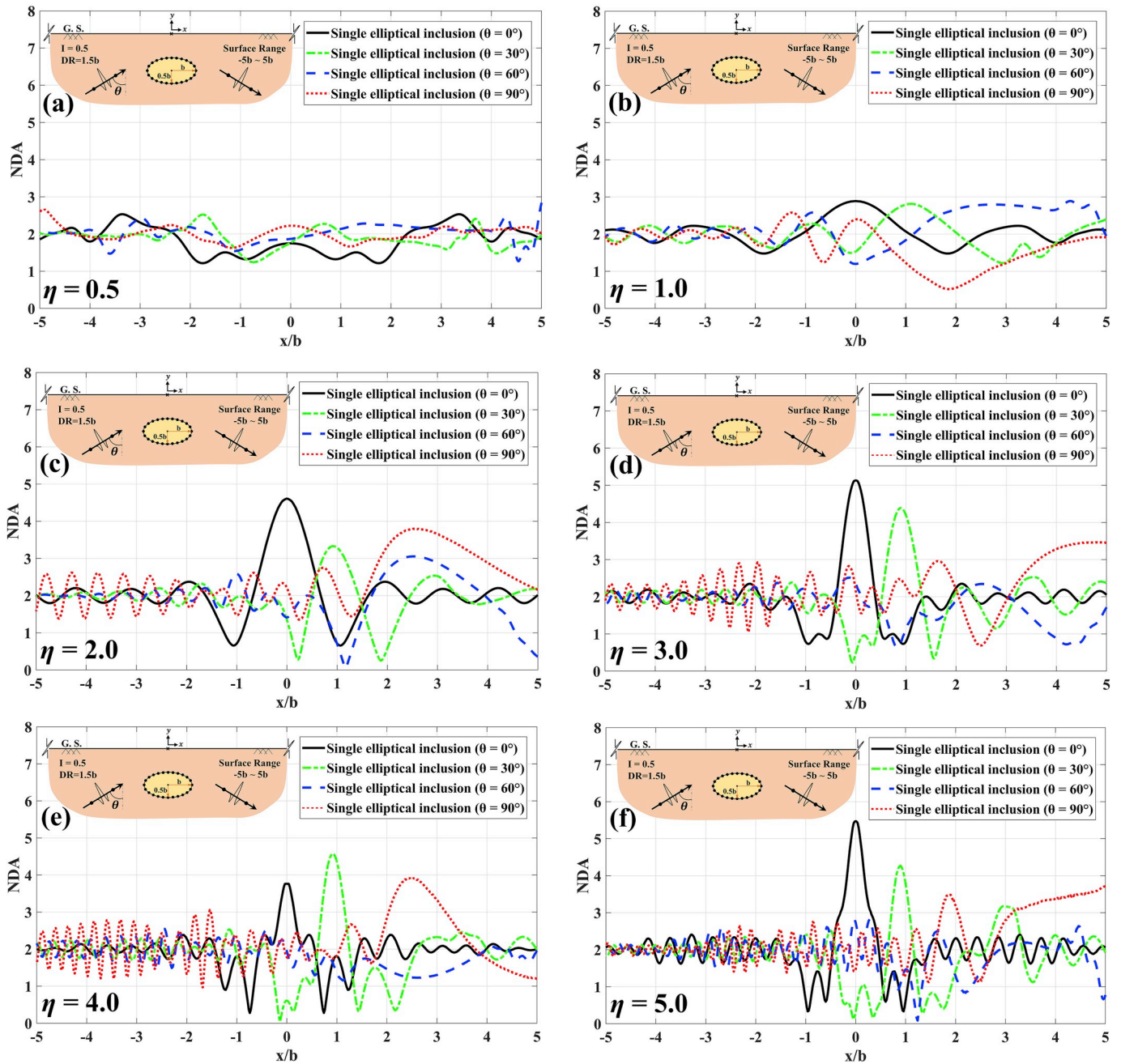
Fig. 23. The normalized displacement amplitude of the ground surface versus x/b for the model of an elliptical inclusion with the radius of *b* subjected to the *SH*-waves with $I = 0.5$, DR = 1.5b for different incident angles and dimensionless frequencies.

full-plane BEM. The depth ratio (DR) is 2.0b, and the incident angles (θ) are $0°$ and $90°$, respectively. Moreover, the dimensionless frequencies (η) of 0.5 and 1.0 are considered and the surface range is between $-10b$ and 10b.

7.1.3. Elliptical inclusion

The results of the present study are compared with those presented by Dravinski (1983) by an indirect frequency-domain BEM and for an underground elliptical inclusion. Fig. 9 shows the normalized displacement amplitude (NDA) of the surface in presence of the mentioned topographic feature. Like the previous verification examples, a good agreement between the responses are achieved that shows the suitable performance of the proposed method.

7.2. Time-domain responses

Figs. 10–15 are presented to show the general pattern of responses in time-domain and illustrate the scattering of the *SH*-waves in presence of a single circular/elliptical inclusion. Three stations are marked on the figures by D, R and C which show the paths of the direct, reflected and crawled waves, respectively (Keller, 1962). Based on the mentioned explanations, for the circular inclusion with $I = 0.1$ and $\theta = 0°$, by colliding the waves to the boundary of inclusion, because of the extremely soft content of inclusion compared to the surrounding medium, the most part of the waves is reflected directly from the boundary of inclusion and the other part is crawled on the surface of its boundary and is then reflected after hitting the surface. In fact, when $I = 0.1$, the boundary of inclusion acts like a mirror and does not allow the high volume of the waves to enter into inclusion or leave it extremely fast.

Thus, a small part of the waves is trapped inside inclusion and cannot leave the medium quickly. On the other hand, some parts of the mentioned reflected and crawler waves are trapped between the top boundary of inclusion and ground surface. Therefore, the duration of the convergence time of the results increases when $I = 0.1$. When $I = 0.1$ and $\theta = 30°$, the amplitudes decrease right behind the location of inclusion relative to the direction of the waves front. This effect is also visible for the response of $\theta = 0°$ known as "shadow zone" (Trifunac, 1973). However, in the results of $\theta = 60°$ and $90°$, this phenomenon is stronger and the lower amplitudes are formed behind inclusion. Moreover, when $\theta = 90°$, the effect of the crawler waves on the ground surface is significantly reduced. Thus, the existing of an inclusion with $I = 0.1$ does not allow the waves to cross easily and reach the behind side of inclusion relative to the angle of the incident waves and acts similar to a barrier.

When $I = 0.3$, the stiffness of the inclusion material slightly increases and is to some extent closer to the stiffness of the surrounding medium. Thus, a higher volume of the waves can enter into the medium of inclusion and the volume of the reflected and crawler waves decrease on the boundary of inclusion. Moreover, the lower volume of the waves may be trapped inside inclusion or between the boundary of inclusion and the ground surface. Accordingly, the convergence of the results can be achieved in a shorter time and the reduction effect of inclusion on the amplitudes of the incident waves will be weaker than the previous cases; this will be the main reason for lower reflected and crawler paths amplitudes. By comparing the results of $I = 0.5$ for circular inclusion to lower impedance ratios, one can see the lowest complexity of the responses for $I = 0.5$. Contrary to the previous cases, the existence of inclusion with a stiffness equal to half of the stiffness of the surrounding medium leads to the accumulation and amplification of the amplitudes of the incident waves in the location of inclusion. On the other hand, the amplitude of the reflected and crawler waves is significantly reduced, showing the congruent behavior of the inclusion material alongside the outer medium. Moreover, the weakest effect of the shadow zone is formed behind inclusion which is because of the lowest barrier effect of inclusion for these cases; thus, the convergence can be achievable extremely faster.

By comparing the responses of elliptical and circular inclusion, one can see that the required convergence time is slightly lower for the elliptical case. This difference is because of the specific shape of elliptical inclusions that leads the reflected and crawler waves in the way with lower effects on the ground surface; thus, the trapped waves between inclusion and the ground surface will decrease as well. On the other hand, the smaller medium of elliptical inclusion leads to fewer trapped waves into the medium of inclusion. Like the previous cases, one can see the diminish of waves amplitude on the location of inclusion and the complexity in the response of elliptical inclusion with $I = 0.1$ and $\theta = 0°$ is lower than the circular model. In fact, when the vertical waves hit the below boundary of the elliptical inclusion, the barrier effect of inclusion is stronger than the circular inclusion and the waves cannot crawl on the boundary of inclusion and reach the ground surface properly. In the case of elliptical inclusion with $I = 0.1$ and $\theta = 90°$, one can see the lowest effect of the shadow zone due to existence of inclusion. When I increases to 0.3, the vibrations of synthetic seismograms decrease. Moreover, the lowest amplitudes and required convergence time among the responses relate to the elliptical inclusion with $I = 0.5$.

7.3. Frequency-domain responses

Figs. 16–19 show the 3D amplification patterns for different scenarios. In these figures, the amplification is the ratio of the surface response amplitude to free-field motion. The dimensionless frequency (η) is considered between 0.25 and 4.0. As the results show, for the circular inclusion with $I = 0.3$ and $\theta = 0°$, the form of response is completely symmetric and one can see extremely low values of amplifications around the location of inclusion. When the incident waves collide to the boundary of inclusion, some part of these waves reflected and the other part is refracted inside the medium of inclusion. Moreover, another part of the incident waves crawls on the boundary of inclusion as well and finally reaches the ground surface. Thus, the values of displacements decrease around inclusion, but the reflected and crawled waves are created the amplifications about 1.7, in a certain distance to the inclusion location. Furthermore, in some specific dimensionless frequencies, one can see the signs of high amplification where inclusion is located. This effect is because of the intermittent reflections of the trapped waves inside the medium of inclusion and those which trapped between the top boundary of inclusion and ground surface. By inclination of the waves front to $\theta = 30°$, the response is not symmetric. However, like the previous case, one still can see extremely low amplifications behind the location of inclusion relative to the angle of the waves front. When $\theta = 60°$, the maximum amplifications occur on the side that the incident waves are collided directly and then reflected reversely. These reflected waves due to presence of inclusion encounter the ground surface and increase the amplifications to about 2. However, on the other side of inclusion, the values of amplification are extremely low and an extremely small part of the waves is able to reach there by crawling on the boundary of inclusion. Unlike the case of $\theta = 60°$, in the model of circular inclusion with $\theta = 90°$, one can see the signs for higher amplifications in the behind zone of inclusion. In the case of $\theta = 90°$, the circular shape of inclusion is the main reason in simplicity of the reflected waves to reach the surface. On the other hand, the crawler waves are slipped horizontally on the boundary of inclusion and their effect on the amplification is appeared on the behind of inclusion. An important note in the cases of circular inclusion with $I = 0.3$, is the value of maximum amplifications which are almost identical for different wave's angles, but in $\theta = 60°$ and $\theta = 90°$, the maximum amplification is a slightly bit more than the other angles and it is recorded about 2.4.

By increasing the impedance ratio to $I = 0.5$, the more volume of the incident waves can enter inside inclusion and the volume of the reflected and crawler waves on the boundary of inclusion decreases. Therefore, the main reason in forming the maximum amplification in these cases, is the intermittent reflections of the incident waves inside inclusion. However, by taking a slightly distance from the middle point of the surface, the values of amplifications are extremely low. When θ is inclined to $60°$, the form of obtained response is relatively similar to the result of $I = 0.3$ for the same case, but the main difference is the effect of the shadow zone which has been reduced when $I = 0.5$. Moreover, by comparing the responses of $\theta = 90°$ for $I = 0.3$ and $I = 0.5$ for circular case, one can see that the barrier effect of inclusion on the path of the incident waves decreases when $I = 0.5$; thus, the dispersion of the incident waves in presence of a circular inclusion with $I = 0.5$ decreases and the values of amplification are lower as well. Moreover, unlike the responses of $I = 0.3$, the maximum amplification in $I = 0.5$ cases is occurred in $\theta = 0°$ and it is higher than the maximum value of $I = 0.3$ and recorded about to 2.7.

In the 3D amplification patterns of elliptical inclusion for $I = 0.3$, the main differences in amplifications and vibrations of the surface are because of the specific shape of elliptical inclusion which cannot create the uniform paths of the reflected and crawled waves with a strong impact. In fact, the wide and smaller medium of elliptical inclusion increases the volume of the trapped waves inside inclusion; thus, the separate vibrations are obtained in 3D diagram in which they do not follow the specific paths. This effect is extremely clear in the case of $I = 0.3$ and $\theta = 0°$. By inclination of the wave's front to reach the horizon, the paths for the crawler waves are easily formed on the boundary of inclusion that weakening the effect of the shadow zone and the waves can reach the behind zone of inclusion by crawling on it. In the following, the NDA responses of the mentioned models are illustrated for

the dimensionless-frequencies of 0.5, 1.0, 2.0, 3.0, 4.0 and 5.0, respectively. Presenting the mentioned 2D diagrams is the best way to see the maximum displacement amplitudes of the surface for separate dimensionless frequencies and compare them for different scenarios. Thus, Figs. 20–23 are presented for these purposes. As the figures show, the lowest vibrations are recorded for circular and elliptical inclusion in $I = 0.5$ and $\eta = 0.5$. However, by increasing the (η) values, the complexity of diagrams increases too. The responses of $\theta = 0°$ in different cases are symmetric. Moreover, the maximum NDA values is obtained in $I = 0.5$ and in high η values, which is about 5.5 in both the circular and elliptical cases.

8. Conclusion

In this paper, a numerical approach called as direct half-plane time-domain BEM was developed and utilized for seismic analysis of the ground surface in presence of arbitrarily shaped subsurface inclusions, subjected to propagating obliquely incident plane *SH*-waves. In the use of mentioned method, the interface of inclusion connected to surrounding domain was only discretized to establish the model. First, with the help of the sub-structuring process, the problem was decomposed into a pitted half-plane and a closed filled solid. After applying the method to each part of the model and subsequently obtaining all matrices, the coupled matrix was determined by satisfying continuity conditions at the interface. Finally, the boundary values including displacements/tractions were obtained by solving the final equation in the time-domain. The method was implemented in developing the algorithm of DASBEM. The precision of the method was investigated by analyzing several examples and comparing the results with those of the published works. The appropriate agreement and high accuracy of the proposed method were visible in diagrams. Then, to complete the results, some graphs of the ground surface were presented for subsurface circular/elliptical soft inclusions as synthetic seismograms, amplification patterns and displacements of the ground surface. Although, the proposed method was utilized to analyze the ground response on the geotechnical earthquake engineering, inclusion problems are always one of the most important problems in mechanical engineering to investigate the composite materials. Therefore, the use of method is practically proposed to researchers who are focused their investigations on the time-history analysis of such materials with arbitrarily shaped multiple inclusions. The results of the present paper can be summarized as follows:

1 By preparing the simple models, half-plane time-domain BEM was available for time-history step-by-step seismic analysis of the ground surface in presence of arbitrarily shaped subsurface inclusions.
2 By comparing the responses of underground cavity alongside inclusion, it can be observed that the role of subsurface soft inclusion was weaker on the seismic isolation and create the safe area on the ground surface.
3 Synthetic seismograms of the surface showed that by increasing the angle of the incident waves, the direct impact of the waves on the surface decreased and the path of direct waves distanced from the reflected and crawled waves paths. When the impedance ratio (I) was extremely low, the amplitudes decreased in the behind side of inclusion relative to the direction waves front known as "shadow zone" and the strongest effect of this phenomenon was emerged when $I = 0.1$.
4 When the geometry of inclusion was circular, the uniform paths of the reflected and crawled waves were formed with a great impact on the ground surface. However, the wide and small shape of elliptical inclusion did not allow the waves to crawl on the boundary of inclusion simply; thus, the occurrence of amplifications was because of increasing the volume of the trapped waves inside the medium of inclusion.

5 The amplification patterns of the surface showed that increasing the angle of the incident waves affected the fluctuations on the side of the incoming wave front. In the cases of $I = 0.5$ and the incident angles of $\theta = 0°$ and $\theta = 30°$, the maximum amplifications were observed right above inclusion. However, the areas far from the incoming waves front were amplified in the cases of $\theta = 60°$ and $\theta = 90°$. Moreover, the maximum recorded displacement value of the ground surface was related to the $I = 0.5$ and high η values for both the circular and elliptical cases.

Author contribution

Mehdi Panji proposed the basic idea, performed the formulation and implemented it into his comprehensive advanced algorithm previously named DASBEM.

Saeed Mojtabazadeh-Hasanlouei prepared the numerical models, performed the advanced parametric study and graphical processing of the figures.

Farshid Yasemi was assistant in model preparation and numerical study.

Appendix A. Supplementary data

Supplementary data to this article can be found online at https://doi.org/10.1016/j.cageo.2019.104342.

References

Ahmad, S., Banerjee, P.K., 1988. Multi-domain BEM for two-dimensional problems of elastodynamics. Int. J. Numer. Methods Eng. 26 (4), 891–911.

Aki, K., 1988. Local site effects and strong ground motion. In: Proceedings of the Special Conference on Earthquake Engineering and Soil Dynamics, vol. 2. American Society of Civil Engineers, Park City, UT.

Aki, K., 1993. Local site effects on weak and strong ground motion. Tectonophysics 218 (1–3), 93–111.

Boore, D.M., 1972. A note on the effect of simple topography on seismic *SH*-waves. Bull. Seismol. Soc. Am. 62, 275–284.

Belytschko, T., Chang, H.S., 1988. Simplified direct time integration boundary element method. J. Eng. Mech. Am. Soc. Civ. Eng. 114 (1), 117–134.

Brebbia, C.A., Dominguez, J., 1989. Boundary Elements, an Introductory Course. Computational Mechanics, Southampton, Boston.

Benites, R., Aki, K., Yomigida, K., 1992. Multiple scattering of *SH*-waves in 2-D media with many cavities. Pure Appl. Geophys. 138, 353–390.

Ba, Z., Yin, X., 2016. Wave scattering of complex local site in a layered half-space by using a multidomain IBEM: incident plane *SH*-waves. Geophys. J. Int. 205 (3), 1382–1405.

Davis, L.L., West, L.R., 1973. Observed effects of topography on ground motion. Bull. Seismol. Soc. Am. 63 (1), 283–298.

Dravinski, M., 1983. Ground motion amplification due to elastic inclusion in a half-space. Earthq. Eng. Struct. Dyn. 11, 313–335.

Dominguez, J., 1993. Boundary Elements in Dynamics. Computational Mechanics, Southampton, Boston.

Dong, C.Y., Lo, S.H., Cheung, Y.K., 2004. Numerical solution for elastic half-plane inclusion problems by different integral equation approaches. Eng. Anal. Bound. Elem. 28, 123–130.

Dravinski, M., Yu, M.C., 2011. Scattering of plane harmonic *SH*-waves by multiple inclusions. Geophys. J. Int. 186, 1331–1346.

Dravinski, M., Sheikhhassani, R., 2013. Scattering of a plane harmonic *SH*-wave by a rough multilayered inclusion of arbitrary shape. Wave Motion 50, 836–851.

Feng, Y.D., Wang, Y.S., Zhang, Z.M., 2003. Transient scattering of *SH*-waves from an inclusion with a unilateral frictional interface, a 2D time domain boundary element analysis. Commun. Numer. Methods Eng. 19, 25–36.

Garcia-Sanchez, F., Zhang, C., 2007. A comparative study of three BEM for transient dynamic crack analysis of 2-D anisotropic solids. Comput. Mech. 40 (4), 753–769.

Hadley, P.K., Askar, A., Cakmak, A.S., 1989. Scattering of Waves by Inclusions in a Nonhomogeneous Elastic Half Space Solved by Boundary Element Methods. Technical Report: NCEER-89-0027.

Huang, Y., Crouch, S.L., Mogilevskaya, S.G., 2005. A time domain direct boundary integral method for a viscoelastic plane with circular holes and elastic inclusions. Eng. Anal. Bound. Elem. 29, 725–737.

Huang, L., Liu, Z., Wu, C., Liang, J., 2019. The scattering of plane P, SV waves by twin lining tunnels with imperfect interfaces embedded in an elastic half-space. Tunn. Undergr. Space Technol. 85, 319–330.

Keller, J.B., 1962. Geometrical theory of diffraction. J. Opt. Soc. Am. 52 (2), 116–130.

Kawase, H., 1988. Time-domain response of a semi-circular canyon for incident *SV, P* and *Rayleigh*-waves calculated by the discrete wave-number boundary element method. Bull. Seismol. Soc. Am. 78 (4), 1415–1437.

Kawase, H., Sato, T., 1992. Simulation analysis of strong motions in the Ashigara valley considering one- and two-dimensional geological structures. J. Phys. Earth 40, 27–56.

Kamalian, M., Gatmiri, B., Sohrabi-Bidar, A., 2003. On time-domain two-dimensional site response analysis of topographic structures by BEM. J. Earthq. Eng. 5 (2), 35–45.

Kamalian, M., Jafari, M.K., Sohrabi-Bidar, A., Razmkhah, A., Gatmiri, B., 2006. Time-domain two-dimensional site response analysis of non-homogeneous topographic structures by a hybrid FE/BE method. Soil Dyn. Earthq. Eng. 26 (8), 753–765.

Lysmer, J., Drake, L.A., 1972. A Finite Element Method for Seismology. Methods of Computational Physics, vol. 11. Academic Press, New York, pp. 181–216.

Lee, V.W., 1977. On the deformations near circular underground cavity subjected to incident plane *SH*-waves. In: Conference Proceedings of Application of Computer Methods in Engineering, vol. 9. University of South California, Los Angeles, pp. 51–62.

Lubich, C., 1988. Convolution quadrature and discretized operational calculus. I. Numerische Mathematik 52 (2), 129–145.

Luco, J.E., de Barros, F.C.P., 1994. Dynamic displacements and stresses in the vicinity of a cylindrical cavity embedded in a halfspace. Earthq. Eng. Struct. Dyn. 23, 321–340.

Liang, J., Liu, Z., Huang, L., Yang, G., 2019. The indirect boundary integral equation method for the broadband scattering of plane P, SV and Rayleigh waves by a hill topography. Eng. Anal. Bound. Elem. 98, 184–202.

Moczo, P., Bard, P.Y., 1993. Wave diffraction, amplification and differential motion near strong lateral discontinuities. Bull. Seismol. Soc. Am. 83, 85–106.

Manoogian, M.E., Lee, V.W., 1996. Diffraction of *SH*-waves by subsurface inclusion of arbitrary shape. J. Eng. Mech. 122 (2), 123–129.

Mykhaskiv, V., 2005. Transient response of a plane rigid inclusion to an incident wave in an elastic solid. Wave Motion 41, 133–144.

Manolis, G.D., Dineva, P.S., Rangelov, T.V., Wuttke, F., 2017. Seismic Wave Propagation in Non-homogeneous Elastic Media by Boundary Elements, vol. 240. Springer, p. 294. https://doi.org/10.1007/978-3-319-45206-7. Series, Solid Mechanics and Its Applications.

MATLAB, 2018. The Language of Technical Computing. The MathWorks Inc, Natick, Massachusetts, Version 9.4.

Ohtsuki, A., Harumi, K., 1983. Effects of topography and subsurface inhomogeneities on seismic *SV*-waves. Earthq. Eng. Struct. Dyn. 11, 441–462.

Panji, M., Asgari Marnani, J., Tavousi Tafreshi, S.H., 2011. Evaluation of effective parameters on the underground tunnel stability using BEM. J. Struct. Eng. Geo- Tech. 1 (2), 29–37.

Panji, M., Kamalian, M., Asgari Marnani, J., Jafari, M.K., 2013. Transient analysis of wave propagation problems by half-plane BEM. Geophys. J. Int. 194 (3), 1849–1865.

Panji, M., Kamalian, M., Asgari Marnani, J., Jafari, M.K., 2014. Analyzing seismic convex topographies by a half-plane time-domain BEM. Geophys. J. Int. 197 (1), 591–607.

Panji, M., Kamalian, M., Asgari Marnani, J., Jafari, M.K., 2014. Antiplane seismic response from semi-sine shaped valley above embedded truncated circular cavity: a time-domain half-plane BEM. Int. J. Civ. Eng. 12 (2), 193–206.

Parvanova, S.L., Dineva, P.S., Manolis, G.D., Kochev, P.N., 2014. Dynamic response of a solid with multiple inclusions under anti-plane strain conditions by the BEM. Comput. Struct. 139, 65–83.

Parvanova, S.L., Manolis, G.D., Dineva, P.S., 2015. Wave scattering by Nano-heterogeneities embedded in an elastic matrix via BEM. Eng. Anal. Bound. Elem. 56, 57–69.

Panji, M., Koohsari, H., Adampira, M., Alielahi, H., Asgari Marnani, J., 2016. Stability analysis of shallow tunnels subjected to eccentric loads by a boundary element method. J. Rock Mech. Geotech. Eng. 8, 480–488.

Panji, M., Ansari, B., 2017. Modeling pressure pipe embedded in two-layer soil by a half-plane BEM. Comput. Geotech. 81, 360–367.

Panji, M., Ansari, B., 2017. Transient *SH*-waves scattering by the lined tunnel embedded in elastic half-plane. Eng. Anal. Bound. Elem. 84, 220–230.

Panji, M., Mojtabazadeh-Hasanlouei, S., 2018. Time-history responses on the surface by regularly distributed enormous embedded cavities: incident *SH*-waves. Earthq. Sci. 31, 1–17.

Panji, M., Mojtabazadeh-Hasanlouei, S., 2020. Transient response of irregular surface by periodically distributed semi-sine shaped valleys: incident *SH*-waves. J. Earthq. Tsunami. https://doi.org/10.1142/S1793431120500050.

Ricker, N., 1953. The form and laws of propagation of seismic wavelet. Geophysics 18 (1), 10–40.

Rice, J.M., Sadd, M.H., 1984. Propagation and scattering of *SH*-waves in semi-infinite domains using a time-dependent boundary element method. Am. Soc. Mech. Eng. 51, 641–645.

Reinoso, E., Wrobel, L.C., Power, H., 1993. Preliminary results of the modeling of the Mexico City valley with a two-dimensional boundary element method for the scattering of *SH*-waves. Soil Dyn. Earthq. Eng. 12 (8), 457–468.

Sánchez-Sesma, F.J., 1987. Site effects on strong ground motion. Soil Dyn. Earthq. Eng. 6 (2), 124–132.

Sánchez-Sesma, F.J., Palencia, V.J., Luzón, F., 2002. Estimation of local site effects during earthquakes: an overview. ISET J. Earthq. Technol. 39 (3), 167–193.

Trifunac, M.D., 1973. Scattering of plane *SH*-waves by a semi-cylindrical canyon. Earthq. Eng. Struct. Dyn. 1, 267–281.

Smith, W.D., 1975. The application of finite element analysis to body wave propagation problems. Geophys. J. R. Astron. Soc. 42 (2), 747–768.

Takemiya, H., Fujiwara, A., 1994. *SH*-wave scattering and propagation analyses at irregular sites by time domain BEM. Bull. Seismol. Soc. Am. 84 (5), 1443–1455.

Yuan, X., 1996. Effect of a circular underground inclusion on surface motion under incident plane *SH*-waves. Acta Geophysica Sinica 39 (3), 373–381.

Zhang, N., Zhang, Y., Gao, Y., Pak, R., Yang, J., 2019. Site amplification effects of a radially multi-layered semi-cylindrical canyon on seismic response of an earth and rockfill dam. Soil Dyn. Earthq. Eng. 116, 145–163.